

RSMC Tokyo - Typhoon Center

Technical Review

No. 13

Contents

Estimation of Tropical Cyclone Intensity Using Aqua/AMSR-E Data	1
Quantitative Precipitation Estimation and Quantitative Precipitation Forecasting (QPE/QPF) by the Japan Meteorological Agency	37

Japan Meteorological Agency

March 2011

PREFACE

The RSMC Tokyo - Typhoon Center provides a variety of tropical cyclone information products to National Meteorological and Hydrological Services (NMHSs) on a real-time basis in order to support tropical cyclone forecasting and disaster preparedness and prevention activities. The Center also issues *RSMC Tropical Cyclone Best Track* and *Annual Report on the Activities of the RSMC Tokyo - Typhoon Center* every year. In addition to these regular publications, it also occasionally publishes its *Technical Review* to outline the achievements of research and development on operational meteorological services related to tropical cyclones.

This issue of *Technical Review No. 13* features the two important topics, namely Estimation of Tropical Cyclone Intensity Using Aqua/AMSR-E Data and Quantitative Precipitation Estimation and Quantitative Precipitation Forecasting (QPE/QPF) by the Japan Meteorological Agency. The former outlines the estimation of tropical cyclone intensity using microwave sensors which is expected to provide objectively analyzed tropical cyclone information complementing traditionally-used Dvorak analysis. The latter describes the JMA's quantitative estimation and forecasting of precipitation which will provide one of the most important information to prepare and prevent possible disasters caused by heavy rain.

The RSMC Tokyo - Typhoon Center hopes this issue will serve as a useful reference for NMHSs in enhancing disaster prevention activities.

Estimation of Tropical Cyclone Intensity Using Aqua/AMSR-E Data

Shiro Yoshida¹, Makoto Sakai¹, Akiko Shouji², Masaya Hirohata³, Akihiro Shimizu⁴

¹ Forecast Division, Forecast Department, JMA

² Sapporo District Meteorological Observatory, JMA

³ Hachijojima Airport Branch, JMA

⁴ Satellite Program Division, Observations Department, JMA

Abstract

In this study, the technique of Hoshino and Nakazawa (2007) was adopted to estimate tropical cyclone (TC) intensity using microwave imagery from the AMSR-E (Advanced Microwave Scanning Radiometer for EOS) sensor on board NASA's Aqua satellite. The results showed a close correlation with the best track data determined by the Japan Meteorological Agency, and it was found that these data could be fully utilized as reference for intensity analysis. Higher levels of objectivity and accuracy in such analysis can be expected by using this data to complement regular intensity analysis with the Dvorak method.

1. Introduction

Surface observations on land and sea, geostationary meteorological satellite imagery and data from microwave scatterometers (such as the SeaWinds sensor on board the QuikSCAT satellite) are mainly used for TC intensity analysis. However, the amounts of TC data available are limited, and more often than not they relate to areas over the sea. Analysis results obtained using the Dvorak method (Dvorak [1975, 1984]) for TC intensity estimation with geostationary meteorological satellite imagery may therefore serve as an important basis for TC intensity analysis. In the Dvorak method, however, erroneous judgment in the developing stage may create significant inaccuracies in the results of such analysis. Accordingly, analysts must take a TC's life stage into consideration when determining its intensity. To avoid erroneous results caused by the subjective judgment of analysts, a skilled analysis technique is required. Additionally, since the Dvorak method involves statistical procedures, analysis of exceptionally rapid development/weakening can be difficult. For all these reasons, establishing a basis to ascertain TC intensity other than analysis using the Dvorak method is expected to enable intensity estimation with a higher level of objectivity. This article covers and reports on the verification of TC intensity estimation using microwave imagery from the AMSR-E sensor on board the Aqua earth observation satellite using the technique of Hoshino and Nakazawa (2007).

2. Research method

2.1 Analytical tool and approach used in the research

GMSLPM/SATAID was used as the analytical tool. SATAID (Satellite Animation and Interactive Diagnosis) is a piece of software that enables PC-based satellite image analysis with a lot of functions such as displaying animation of satellite images, measuring brightness temperature and the like, as well as superimposing various meteorological data. (Meteorological Satellite Center [1999], Kumabe [2000], Kumabe [2001]). For this research, GMSLPM (a version of the SATAID capable of displaying microwave imagery) was selected.

The method of Hoshino and Nakazawa (2007) was adopted for intensity estimation. This technique uses brightness temperature distribution in the microwave frequency band of the TMI sensor on board the TRMM earth observation satellite (referred to hereafter as “TRMM/TMI”). Hoshino and Nakazawa (2007) created a formula for computation based on data collected from 1999 through 2003, and verified it using data gathered from the western North Pacific in 2004. For this verification, Hoshino used data collected from 2002 through 2004 and the same technique, with the parameters recalculated for the AMSR-E sensor on board the Aqua satellite (referred to hereafter as “Aqua/AMSR-E”), and also conducted verification using data from 2005.

Specifically, parameters such as the concentric circle/concentric annulus around the center (the parameter calculation area is that within a radius of two degrees from the TC center), the minimum/maximum/average brightness temperature and the ratio of pixels exceeding a certain threshold level were calculated based on the predetermined TC center position, and candidate values for maximum wind speed (V_{max}) were calculated using 10 regression formulas obtained from known data. The average of these candidate values was then taken as the maximum wind speed. There are two types of estimated maximum wind speed: One is calculated with the maximum wind speed from western North Pacific best track data as a known value (BT_WP), and the other is calculated with the maximum wind speed of data from the global microwave scatterometer (the SeaWinds sensor on board QuikSCAT, hereafter referred to as “QuikSCAT/SeaWinds”) as a known value (SCAT_ALL). Table 1-1 shows the formula for obtaining candidates for the maximum wind speed (V_{max}) as well as the parameters for the regression formula, and Table 1-2 describes the parameters.

In the GMSLPM satellite image display analysis software chosen for this research, 10 candidate maximum wind speed values obtained using the above-mentioned 10 regression formulas (BT_WP and SCAT_ALL) and the average values (BT_WP_Ave and SCAT_ALL_Ave) can be obtained by clicking the TC center position estimated on the Aqua/AMSR-E image shown on the computer screen. An analysis example using GMSLPM is shown in Figure 1.

Table 1-1 Regression formula used to calculate 10 candidate values for maximum wind speed (Vmax), and combinations of coefficients and parameters for calculating BT_WP (top) and SCAT_ALL (bottom)

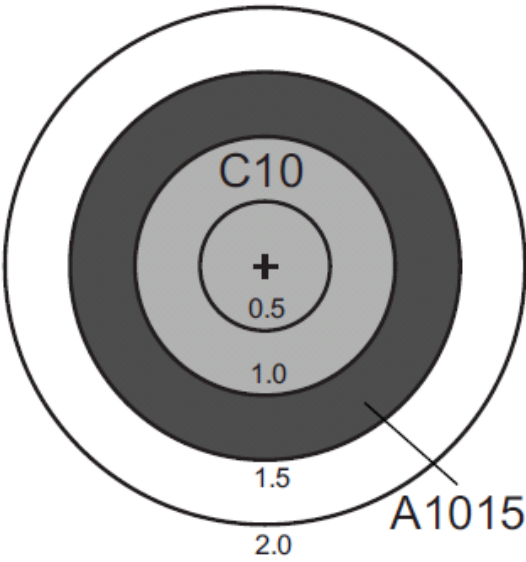
Regression formula used to obtain candidate values for maximum wind speed:

$$V_{max} = aP1 + bP2 + cP3 + d$$

	a	P1	b	P2	c	P3	d
1	0.099	TB07H_AREA110_C10	0.31	TB07V_MIN_C05	0.29	TB10H_MIN_A0515	-59.48
2	0.19	TB07H_AREA110_C10	0.42	TB10H_MIN_A0515	0.28	PCT89_MEAN_A1020	-97.47
3	0.57	TB07V_MIN_C05	0.36	TB10H_MIN_A0515	0.036	PCT89_MIN_C10	-115.59
4	0.16	TB07H_AREA110_C10	0.38	TB07V_MIN_C05	0.048	PCT89_MIN_C10	-54.04
5	0.13	TB07H_AREA110_C10	0.30	TB10H_MIN_A0515	0.22	TB19V_MIN_C05	-55.29
6	0.12	TB07H_AREA110_C10	0.37	TB07V_MIN_C05	0.21	TB24H_MIN_A1015	-90.43
7	0.25	TB07H_AREA110_C10	0.20	TB19H_MEAN_A1520	0.43	PCT89_MEAN_A1020	-136.12
8	0.12	TB07H_AREA110_C10	0.37	TB07V_MIN_C05	0.10	TB19H_MEAN_A1520	-62.86
9	0.52	TB07V_MIN_C05	0.38	TB10H_MIN_A0515	0.034	PCT89_MIN_A1020	-108.86
10	0.50	TB07V_MIN_C05	0.52	TB10H_MIN_A0515	0.18	PCT89_MEAN_A1020	-161.25

	a	P1	b	P2	c	P3	d
1	1.30	TB07H_MEAN_C15	-0.19	TB24H_AREA260_C15	0.32	PCT89_MEAN_C15	-187.65
2	1.10	TB07H_MEAN_C15	-0.15	TB24H_MIN_A1020	0.34	PCT89_MEAN_C15	-143.00
3	0.93	TB07H_MEAN_C15	0.17	TB07V_MAX_C05	0.47	PCT89_MEAN_C15	-227.52
4	1.10	TB07H_MEAN_C15	-0.59	TB07V_MIN_A1020	0.37	PCT89_MEAN_C15	-85.12
5	1.20	TB07H_MEAN_C15	-0.18	TB19H_MIN_A0515	0.38	PCT89_MEAN_C15	-167.22
6	1.10	TB07H_MEAN_C15	-0.15	TB19V_MEAN_A1520	0.37	PCT89_MEAN_C15	-152.32
7	0.99	TB07H_MEAN_C15	0.053	TB19H_MEAN_C05	0.45	PCT89_MEAN_C15	-205.12
8	1.10	TB07H_MEAN_C15	-0.24	TB10V_MIN_A0510	0.34	PCT89_MEAN_C15	-135.98
9	1.00	TB07H_MEAN_C15	-0.15	TB24H_MAX_A1520	0.38	PCT89_MEAN_C15	-142.07
10	1.20	TB07H_MEAN_C15	-0.24	TB24H_AREA260_C15	0.035	PCT89_MIN_A1020	-92.49

Table 1-2 Description of parameters in Table 1-1

Description of Parameters	
TB07H(V):	Brightness temperature according to horizontally (vertically) polarized waves on the 7 GHz band channel
TB10H(V):	Brightness temperature according to horizontally (vertically) polarized waves on the 10 GHz band channel
TB19H(V):	Brightness temperature according to horizontally (vertically) polarized waves on the 19 GHz band channel
TB24H(V):	Brightness temperature according to horizontally (vertically) polarized waves on the 24 GHz band channel
PCT89:	Polarization correction temperature (amount of radiation after deducting that from the sea surface) on the 89 GHz band channel ... $PCT89 = 1.818TB89V - 0.818TB89H$
TB89V:	Brightness temperature of vertically polarized waves
TB89H:	Brightness temperature of horizontally polarized waves
MIN (MAX):	Minimum (maximum) brightness temperature in the area of a concentric circle and concentric annulus around the center
MEAN:	Mean brightness temperature in the area of a concentric circle and concentric annulus around the center
AREA:	Ratio of pixels exceeding a certain threshold value in the area of a concentric circle and concentric annulus around the center
CXX:	Area of a concentric circle around the center with a radius of X.X degrees
AYYZZ:	Area of a concentric annulus around the center with an inside diameter of Y.Y degrees and an outside diameter of Z.Z degrees
(Example 1) TB07H_AREA110_C10: Ratio of pixels for which the brightness temperature is 110 K or more in the area of a concentric circle with a radius of one degree from the center (the light gray part of the figure below) of the horizontally polarized waves on the 7 GHz band channel	
(Example 2) TB10V_MIN_A1015: Minimum brightness temperature in the area of a concentric annulus with a radius of 1.0 to 1.5 degrees from the center (the dark gray part of the figure below) of the vertically polarized waves on the 10 GHz band channel	
 <p>The diagram shows a central point marked with a '+' sign, labeled 'TC center'. Concentric circles are drawn around this center. The innermost circle is labeled 'C10' and has a radius of '0.5'. The next circle out has a radius of '1.0'. The annulus between the 1.0 and 1.5 radius circles is shaded dark gray and labeled 'A1015'. The next circle has a radius of '1.5', and the outermost circle has a radius of '2.0'.</p>	
+ indicates the TC center	

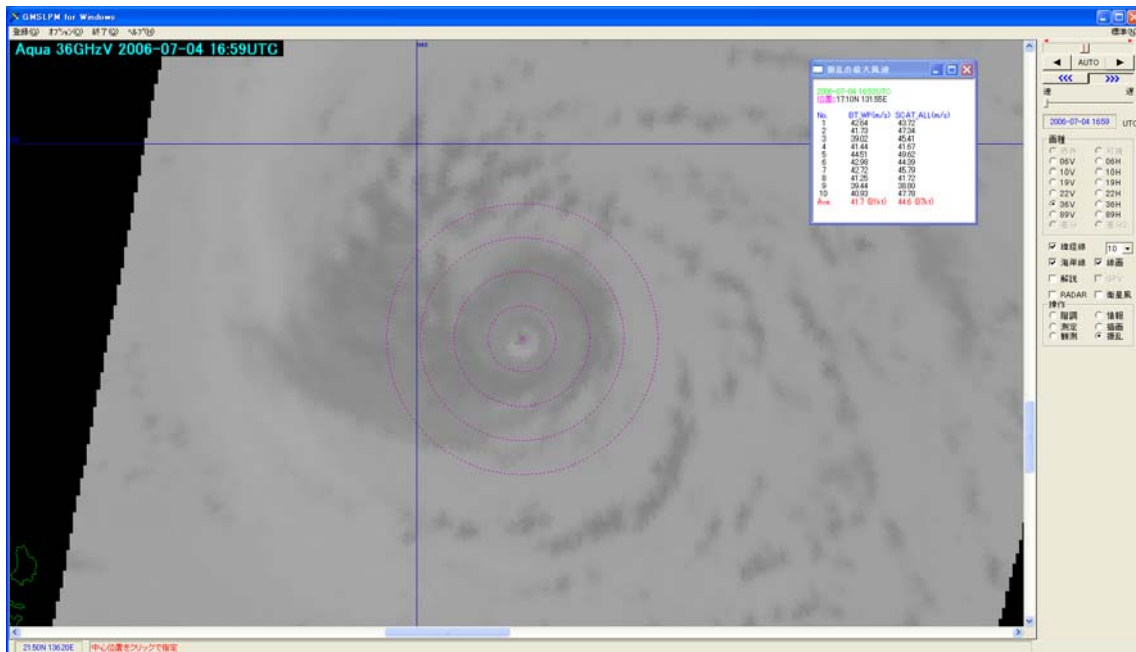


Figure 1 On-screen appearance of GMSLPM satellite image display analysis software (analysis example)

2.2 Targeted TC and methods of research

This research used TCs with TS intensity or higher analyzed as best track between June 2003 and December 2006. The data selected were those recorded while the best track TC center was in the observation range within three hours (before or after) of the Aqua/AMSR-E observation time. As the interval of the best track data covers a maximum of six hours, the time difference between Aqua/AMSR-E observation and the best track must be within three hours. Aqua/AMSR-E observation time here is rounded to the nearest hour.

For the research, images used by the Analysis Division of the Meteorological Satellite Center for TC center analytical investigation involving microwave satellite imagery and the center position obtained at that time (2003 through 2005) were chosen (Nishimura et al. [2007]). The center position was newly determined for Aqua/AMSR-E imagery from 2006. The procedures followed to determine this position were the same as those outlined by Nishimura et al. (2007) (Figure 2). Hoshino and Nakazawa (2007) determined the TC center position for hours without best track data by interpolating the best track, but in this research the center was determined using microwave imagery, which should prove to be more accurate in terms of positioning.

The TC cloud patterns of the microwave images used to estimate the center location were those given by Nishimura et al. (2007), meaning that they were different from those of the Dvorak method. Examples of these patterns are shown in Figure 3. In this report, they are described with the prefix of MW, such as MW EYE, etc. Categorization of TC cloud patterns by the Dvorak method was performed according to “Analysis and use of meteorological satellite images: Tropical cyclones” (Meteorological Satellite Center, 2004).

Knots (KT) were used as the unit of maximum wind speed as with best track data. However, Hoshino and Nakazawa (2007) used m/s in their research, so this unit was used in comparisons for accuracy verification.

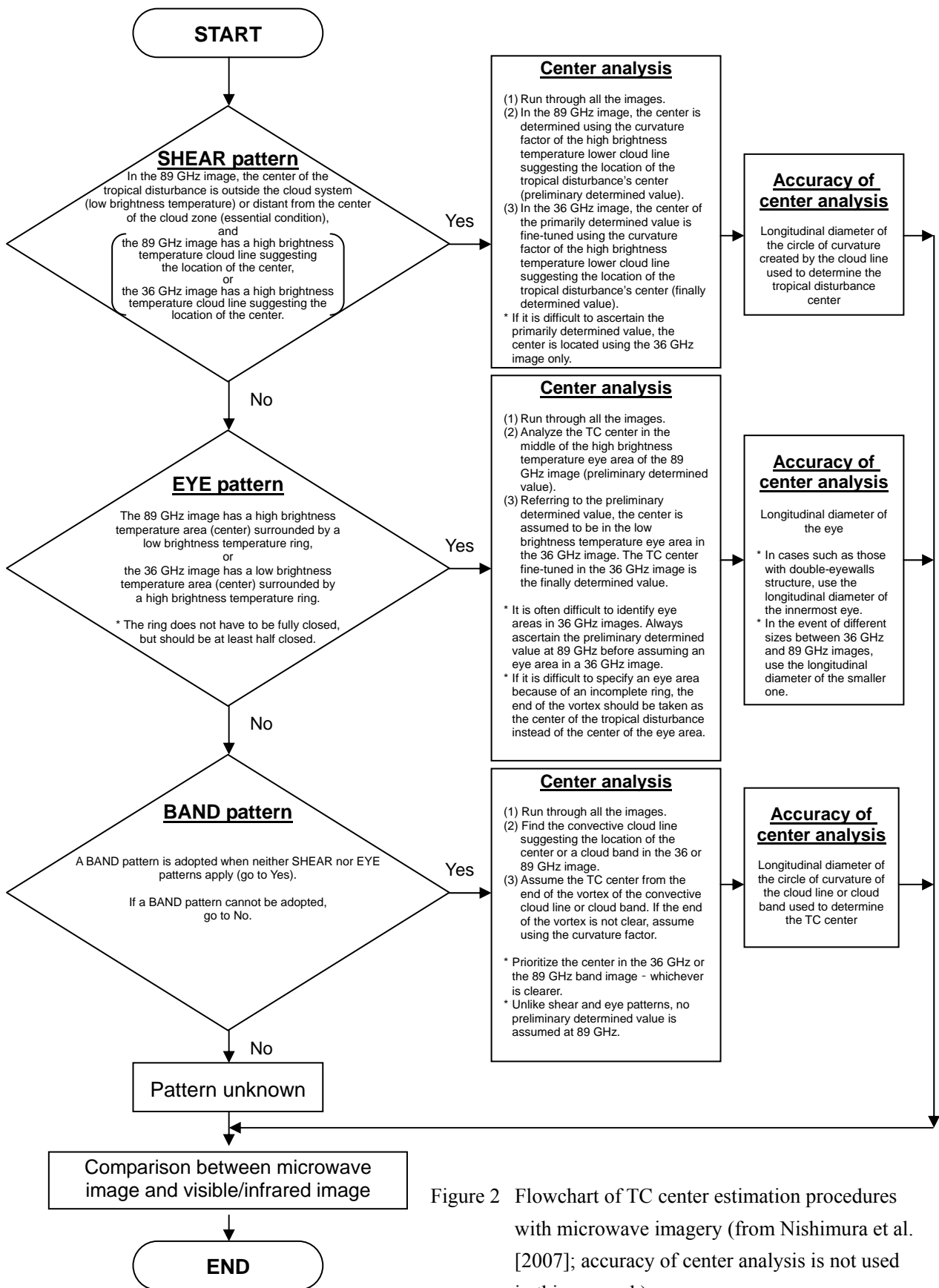
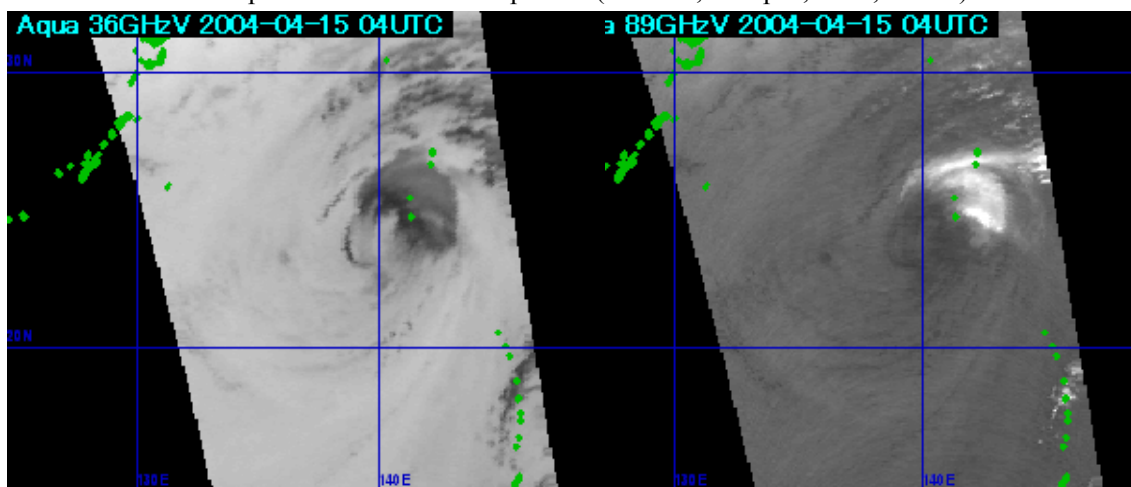
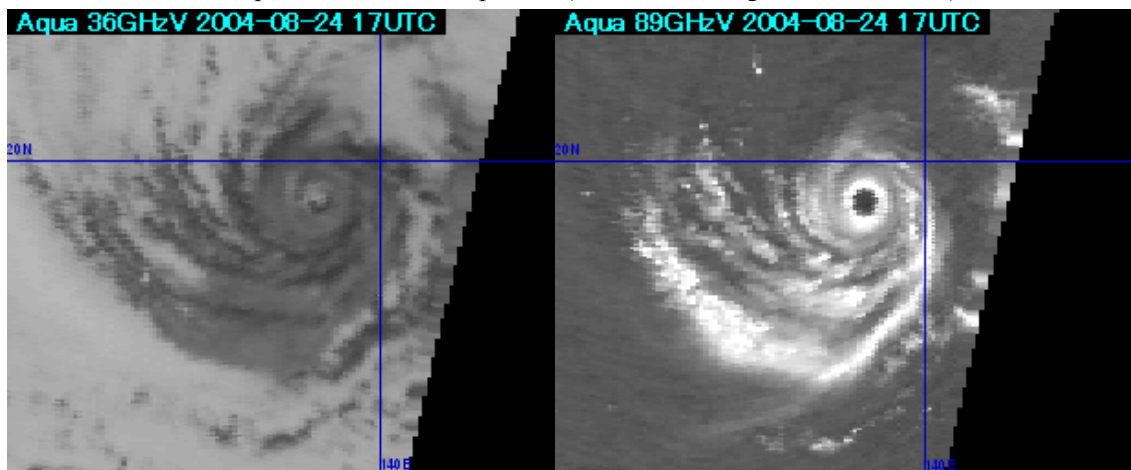


Figure 2 Flowchart of TC center estimation procedures with microwave imagery (from Nishimura et al. [2007]; accuracy of center analysis is not used in this research)

Example of an MW SHEAR pattern (04 UTC, 15 April, 2004, T0401)



Example of an MW EYE pattern (17 UTC, 24 August, 2004, T0416)



Example of an MW BAND pattern (18 UTC, 21 November, 2004, T0425)

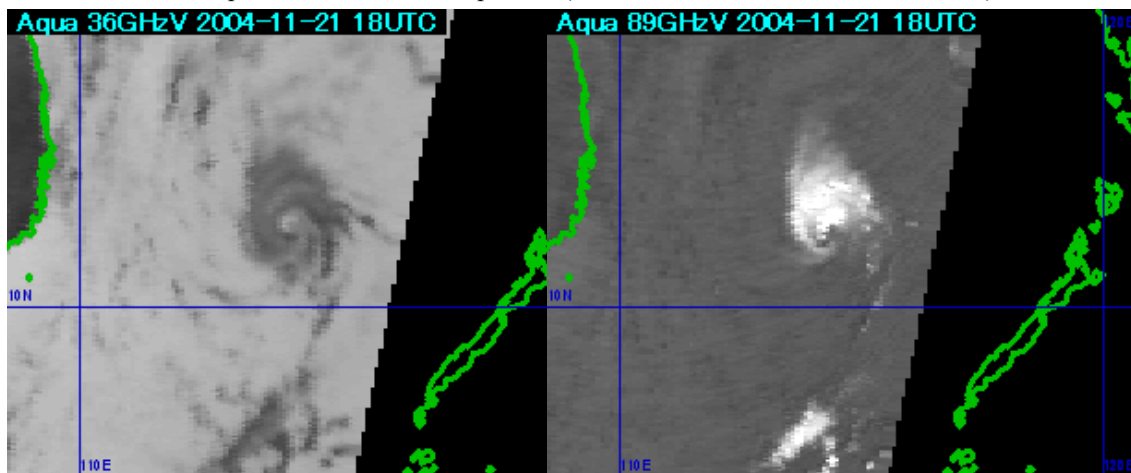


Figure 3 Examples of cloud patterns used to assume TC center locations (36 GHz on the left and 89 GHz on the right)

3. Verification results

In this study, the relationship of the best track maximum wind speed to BT_WP and SCAT_ALL was verified from various perspectives, with the maximum wind speed of the best track in the western North Pacific (as determined by the Japan Meteorological Agency) taken as a true value.

Hoshino and Nakazawa (2007) selected the maximum wind speed from QuikSCAT/SeaWinds within three degrees of latitude from the TC center and calculated SCAT_ALL. As this value is set to approach the maximum wind speed of QuikSCAT/SeaWinds, direct comparison with QuikSCAT/SeaWinds data is necessary for strict verification. However, comparison with the maximum wind speed obtained from QuikSCAT/SeaWinds data was not conducted in this study because only the best track maximum wind speed was used as a true value.

3.1 Scatter diagram of overall data: relationship of best track maximum wind speed to BT_WP and SCAT_ALL

A comparison based on the overall data for 2003 through 2005 is shown in Figure 4 (355 cases for BT_WP_Ave and 353 for SCAT_ALL_Ave). The correlation coefficients of BT_WP_Ave and SCAT_ALL_Ave to the best track maximum wind speed of these data were 0.71 and 0.22, respectively.

There is a relatively good correlation between the best track maximum wind speed and BT_WP, but SCAT_ALL_Ave values are sometimes far higher. Here, if the cases in which SCAT_ALL_Ave is 120 KT or more are excluded, the correlation coefficient becomes 0.72 (figure omitted). There are 34 cases in which SCAT_ALL_Ave is 120 KT or more, and the majority of these (30) had land within two degrees of the typhoon center position. There were also 29 cases in which SCAT_ALL_Ave was 135 KT or more, but all of them included land. This effect of land on data is discussed in the next section.

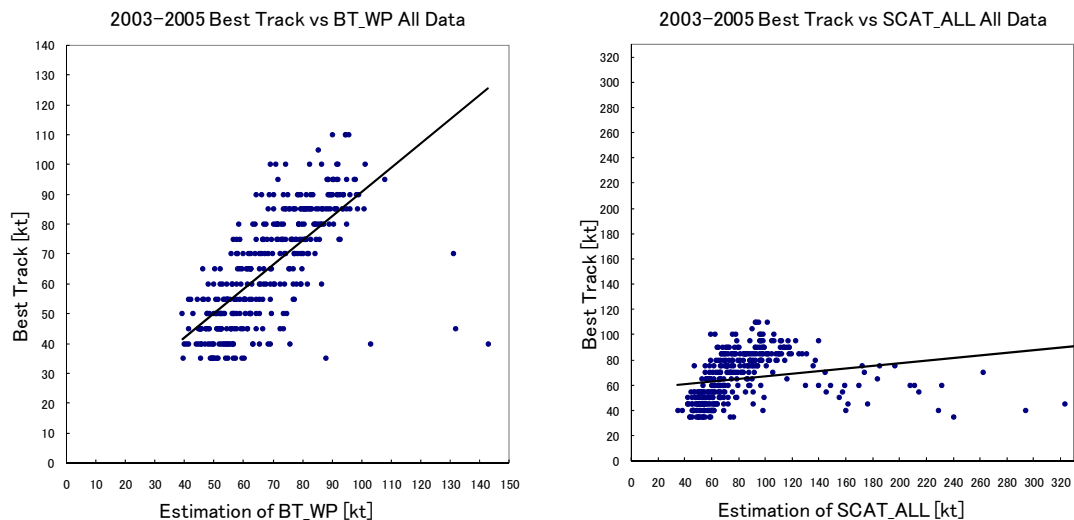


Figure 4 Scatter diagram of overall data for 2003 through 2005
Scatter diagram of best track maximum wind speed and BT_WP_Ave (left)
Scatter diagram of best track maximum wind speed and SCAT_ALL_Ave (right)
The straight line in each figure is the regression line.

3.2 Effect of land

In microwave observation, emissivity is greater on land than over the sea, and the brightness temperature is much higher on land. Figure 5 shows the results of eliminating this land effect by performing calculation after excluding an additional area of one pixel* on the outside (i.e., the sea side) of pixels judged to be land by GMSLPM satellite image display analysis software. Here, two types of data are excluded: those from which BT_WP_Ave cannot be calculated because the land coverage area is too large, and those from which the TC center position cannot be determined due to unclear TC cloud patterns in microwave images. The remaining data from 2003 through 2006 were used; the total number of cases was 470 for BT_WP_Ave and 471 for SCAT_ALL_Ave. (Data from 2006 for which the TC center position was determined in 2008 were included. It is known from the data for 2003 through 2005 that adding cases that include land within two degrees of the TC center position causes a deterioration of the correlation coefficient, so cases including land were excluded from the data for 2006. Verification was conducted using the data for 2003 through 2006 for Section 3.2 onwards.)

As a result of excluding the effect of land, the calculated BT_WP value (which shows an inherently good correlation with and minimal difference from the best track data) includes no values that are exceptionally larger than those of the best track resulting in even better correlation. The correlation coefficients of BT_WP_Ave and SCAT_ALL_Ave to the best track maximum wind speed are now 0.83 and 0.72, respectively, with the calculated SCAT_ALL_Ave value apparently showing a better correlation.

The left part of Figure 5 also shows the tendency for calculation of BT_WP_Ave on the stronger side for a weak best track maximum wind speed and BT_WP_Ave on the weaker side for a strong best track maximum wind speed. This tendency also applies to periods for a tropical depression, a TC with a maximum wind speed of less than 34 KT before development to tropical storm intensity (not included in the research cases of Section 3.3 onwards) in the best track, and BT_WP_Ave was calculated as being stronger during periods of TD status (21 cases during the whole period; table omitted).

Verification results excluding the effect of land are shown below.

* One pixel is approximately 10 km.

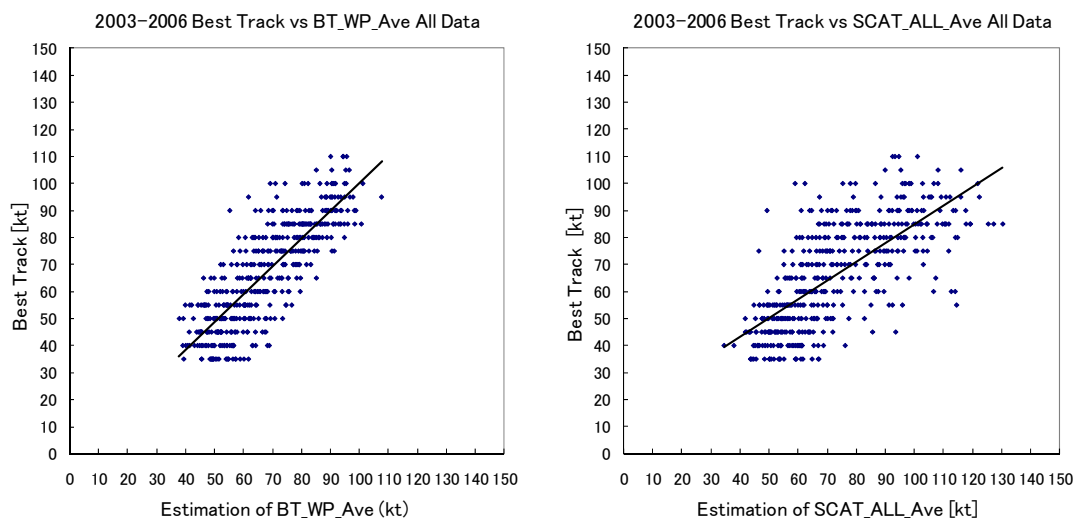


Figure 5 Scatter diagram of overall data for 2003 through 2006 excluding the effect of land
 Scatter diagram of best track maximum wind speed and BT_WP_Ave (left)
 Scatter diagram of best track maximum wind speed and SCAT_ALL_Ave (right)
 The straight line in each figure is the regression line.

3.3 Effect of partially missing imagery in the parameter calculation area or non-calculation of candidate values for maximum wind speed

As the Aqua polar orbiting satellite has a limited observation range, the TC center is not always in the center of the image, and the whole of the parameter calculation area within a two-degree radius of the TC center is not always contained in the image. The data used here have 111 cases of partially missing imagery for the parameter calculation area within a two-degree radius of the TC center. The correlation coefficient between the best track maximum wind speed and BT_WP_Ave with these missing parts is 0.83, which is the same as the corresponding coefficient derived in Section 3.2. As the effect of data with partially missing imagery in the parameter calculation area within a two-degree radius of the TC center is therefore considered insignificant, such data are used.

There are also 15 cases of data* with imagery that is partially missing for the reasons outlined above and data lacking calculation of any one of the maximum wind speed candidate values obtained from the 10 regression formulas due to the effect of land. With these missing data, the correlation coefficient between the best track maximum wind speed and BT_WP_Ave is 0.83, which is the same as the value obtained in Section 3.2 from the same data. As the effect on the calculated BT_WP_Ave value is therefore considered small even if maximum wind speed candidate values cannot be obtained, such data are used (table omitted).

* A specification of the GMSLPM software referenced in this report is that the brightness temperature statistical values of the individual frequency bands used for each regression formula must be valid for more than half the valid pixels in the calculation area. In areas where invalid pixels account for more than half of the total due to partially missing imagery or the

effect of land, the maximum wind speed cannot be obtained using a regression formula (i.e., it cannot be calculated).

3.4 Verification of accuracy by year

The level of error in the average of the 10 candidate values for maximum wind speed against the best track is shown in Table 2. Using the technique for TRMM/TMI imagery, Hoshino modified the parameters to calculate the 10 candidate values for maximum wind speed for Aqua/AMSR-E images, but the research and the algorithm using Aqua/AMSR-E imagery were based on data from 2002 through 2004. In addition, verification was performed using partial data for 2005, so 2006 figures represented independent verification data in this research. As shown in Table 2, a result similar to that found by Hoshino was obtained for BT_WP_Ave. For SCAT_ALL_Ave, on the other hand, the true value was taken as the maximum best track wind speed, and the level of error was greater than that seen in Hoshino's result using the maximum QuikSCAT/SeaWinds wind speed.

Hoshino and Nakazawa (2007) selected the maximum QuikSCAT/SeaWinds wind speed within three degrees of latitude from the TC center and made this the maximum wind speed. As seen so far, the best track maximum wind speed is obtained as the true value, so SCAT_ALL_Ave has a lower correlation than BT_WP_Ave and a greater RMSE. Henceforth, only the comparison between maximum best track wind speed and BT_WP_Ave is to be verified.

Additionally, the number of cases for 2004 (29 TCs) is considered to have been greater than those in other years because 2003 included only cases from June onward, and fewer (23) TCs were recorded for 2005 and 2006 (average value: 26.7 for 1971 – 2000 according to the Japan Meteorological Agency).

Table 2 Accuracy verification results

RMSE of individual years and for overall data (top)

RMSE of Hoshino’s research (bottom; SCAT_ALL_Ave is compared with the maximum wind speed of QuikSCAT data.)

RMSE (m/s)	BT_WP_Ave (no. of cases)	SCAT_ALL_Ave (no. of cases)
2003	5.85 (50)	9.65 (49)
2004	5.22 (189)	8.07 (188)
2005	5.34 (116)	8.36 (116)
2006	6.03 (115)	8.34 (118)
2003 – 2006	5.55 (470)	8.39 (471)

RMSE (m/s)	BT_WP_Ave	SCAT_ALL_Ave
2002 – 2004	5.12	6.20
2005	5.15	5.18

(Total number of cases in the lower table: western North Pacific best track data 351; QuikSCAT data 502)

3.5 Effects of subordinate and independent data

As outlined in Section 3.4, the difference between subordinate data (2003 – 2005) and independent data (2006) in terms of RMSE is some 0.5 m/s. Little difference is found by comparing scatter diagrams between 2004 and 2006 (Figure 6), indicating that the independent 2006 data yield a similar level of calculation accuracy. The correlation coefficients between the best track maximum wind speed and BT_WP were 0.86 for 2004 and 0.81 for 2006.

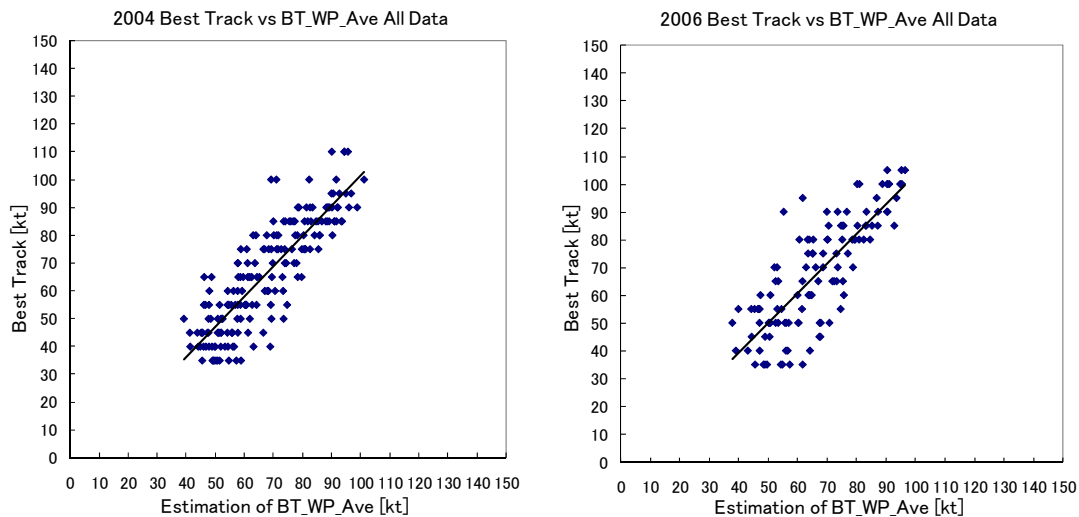


Figure 6 Scatter diagram of best track maximum wind speed and BT_WP for 2004 (left) and 2006 (right). The straight line in each figure is the regression line.

3.6 Differences in cloud patterns and TC comparison among life stages

As shown in Figure 2, if an area of high (low) brightness temperature is surrounded more than halfway around by a ring of low (high) brightness temperature in an 89 GHz (36 GHz) image, it is regarded as an MW EYE pattern from among the TC center estimation patterns of microwave imagery (the area of high [low] brightness temperature looks darker [brighter] in the image of Figure 3). Of these MW EYE patterns, those with a complete ring around the TC eye in images at 89 GHz or 36 GHz are defined as MW TEYE for further segmentation, and the effect caused by the difference in form (pattern) was checked (Figure 7). The results showed that the correlation coefficient between the best track maximum wind speed and BT_WP_Ave was 0.76 for the MW EYE pattern and 0.75 for the MW TEYE pattern, indicating that there was no improvement of accuracy from the segmentation and that the correlation coefficient was almost the same.

The accuracy of BT_WP_Ave classified* into TC life stages (developing, mature and weakening) is shown in Table 3. Classification of TC cloud patterns using the Dvorak method is also shown in Table 4. In determining criteria for the three classifications (Table 3) of developing stage, mature stage and weakening stage, maximum wind speeds of 64 KT or more (the wind speed regarded as “Typhoon” in the TC classification and equivalent to a maritime typhoon warning) or a TC cloud pattern of Eye or Banding Eye according to the Dvorak method (Table 4) were considered to represent the mature stage. Excluded from the mature stage are storms with maximum wind speeds of less than 64 KT. The developing stage is when the T number is equivalent to the CI number (corresponding to the stages of generation to development according to the Dvorak method’s classification), and the weakening stage is when the T number is different from the CI number. The T number is an index indicating TC intensity as obtained from analysis of satellite images according to the Dvorak method, and is adjusted to the CI number. When a TC is developing or has redeveloped, the T number is equivalent to the CI number. That is, the developing stage also includes times when the TC has redeveloped.

As seen in Table 3, the average error between the best track maximum wind speed and BT_WP_Ave in the developing stage is calculated with the best track maximum wind speed stronger, at +4.98 m/s, and the average error of the mature stage is calculated with the best track maximum wind speed weaker, at -1.95 m/s. Better accuracy is seen in the weakening stage than in the other stages.

Figure 8 is a scatter diagram color-coded by the life stages (developing, mature and weakening) outlined in Table 3 and by the TC cloud patterns according to the Dvorak method shown in Table 4. It indicates that there are many instances of Cb Cluster or Curved Band in the developing stage, and that BT_WP_Ave tends to be calculated as stronger than the best track maximum wind speed. In the mature stage, BT_WP_Ave corresponds closely to the best track maximum wind speed, but may be calculated as weaker for the Eye type. Cases with large margins of error are verified in Section 3.11. For the weakening stage, there are many instances of Shear/LCV or Curved Band, and the value calculated is almost the same as the best track maximum wind speed.

* Classification by setting the three TC life stages (developing, mature and weakening) as criteria was implemented to prevent cloud patterns from being included in multiple life stages when the Dvorak method’s TC life stages are used.

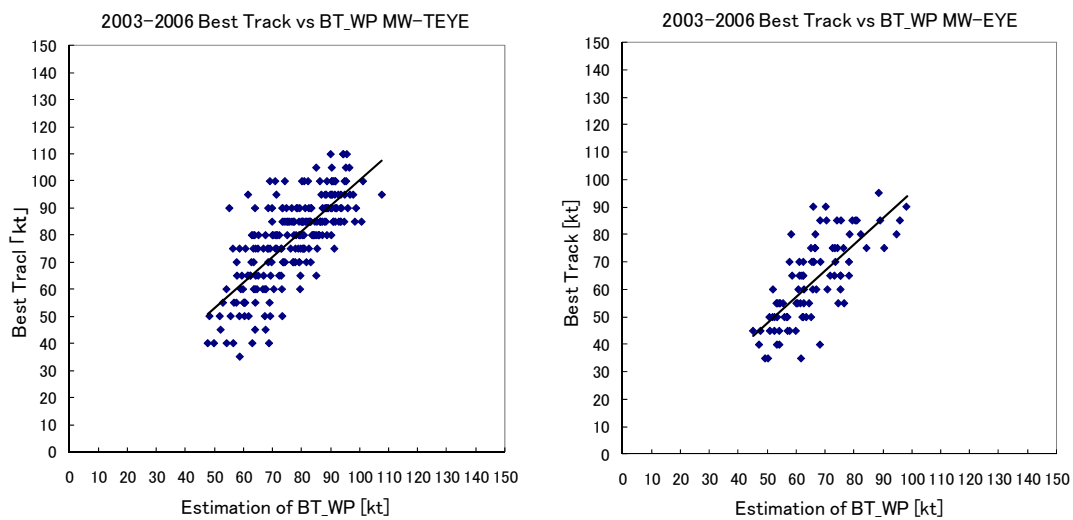


Figure 7 Scatter diagram of best track maximum wind speed and BT_WP_Ave for the microwave imagery TC cloud pattern of MW TEYE (left) and BT_WP_Ave for MW EYE (right) (MW EYE does not include MW TEYE cases.)

The straight line in each figure is the regression line.

Table 3 Accuracy of BT_WP_Ave classified by TC life stage (developing: upper left; mature: upper right; weakening: lower left) (The total number of cases from the developing stage to the weakening stage is 469. There was only one case in which TC analysis was not conducted by the satellite during the target time.)

TC life stage	No. of data	Average of best track maximum wind speed (KT)	Average of BT_WP_Ave (KT)	Average margin of error (m/s)	RMSE (KT)	RMSE (m/s)
Developing	127	47.28	56.97	4.98	12.84	6.60
Mature	262	81.35	77.56	-1.95	10.37	5.33
Weakening	80	50.25	52.18	0.99	8.28	4.26
ALL_DATA	470	66.77	67.61	0.43	10.78	5.55

Table 4 Cloud patterns for TC center estimation using the Dvorak method and their characteristics
 (Source: Analysis and use of meteorological satellite images: Tropical cyclones)

Stage	Cloud pattern	Cloud pattern in typhoon center	Cloud pattern characteristics
Generating	Cb Cluster	Unorganized Cb Cluster	Cb clusters are scattered around the center.
		Organized Cb Cluster	Cb clusters are organized, and transformation to a band pattern is seen.
	LCV	LCV or Shear	Low-level cloud vortex
	Shear		Appears when the vertical shear of the wind is greater and the dense cloud area deviates from the center determined by the low-level cloud line.
Developing	Curved Band	Curved Band	There is a cloud band with a curvature factor suggesting the location of the center.
	CDO	Distinct CDO	An almost-circular dense cloud area (CDO: central dense overcast) surrounds the center with at least one end having a clear edge.
		Indistinct CDO	The CDO boundary is ragged or indistinct.
Mature	Eye	Distinct Small Eye	Eye with a diameter of 40 km or less
		Distinct Large Eye	Eye with a diameter greater than 40 km
		Ragged Eye	The cloud walls forming the eye are either irregularly shaped or include other clouds.
	Banding Eye	Banding Eye	There is more than one cloud band fully surrounding the eye.
Weakening	Curved Band	Curved Band	There is a cloud band with a curvature factor suggesting the location of the center.
	Shear	LCV or Shear	Appears when the vertical shear of the wind is greater and the dense cloud area deviates from the center determined by the low-level cloud line.
	LCV		Low-level cloud vortex
	EXL		Transformation to an extratropical cyclone

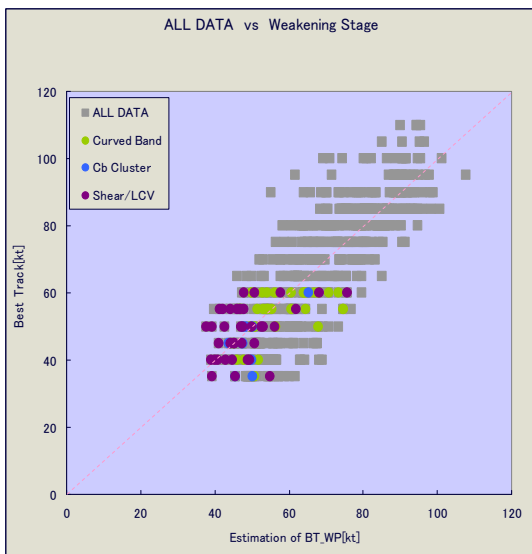
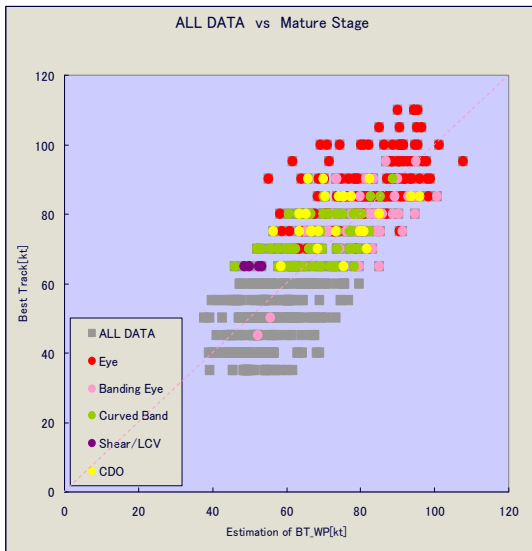
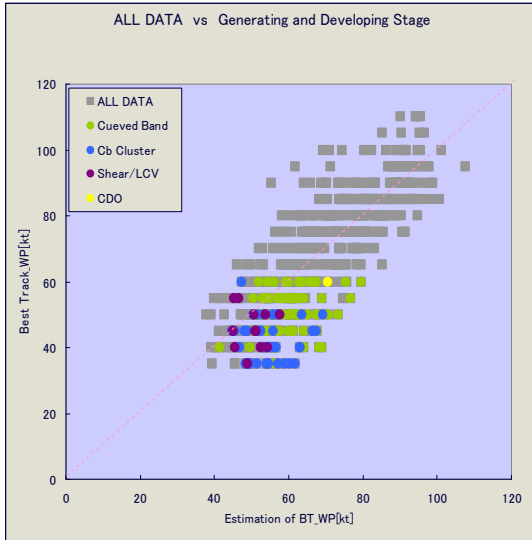


Figure 8
 Scatter diagrams of TC cloud patterns according to the classification of Table 3 (top: best track maximum wind speed and BT_WP_Ave in the developing stage; middle: best track maximum wind speed and BT_WP_Ave in the mature stage; bottom: best track maximum wind speed and BT_WP_Ave in the weakening stage. Explanatory notes are shown in each figure [“Eye,” etc. are as per Dvorak cloud pattern classification]. To facilitate understanding of the correlation tendency, the best track maximum wind speed, or BT_WP_Ave, is indicated with dashed lines.)

3.7 Correlation between best track maximum wind speed and BT_WP for TC cloud patterns in microwave images

For each microwave image TC cloud pattern, the correlation between the best track maximum wind speed and the BT_WP of the 10 candidate values for maximum wind speed and RMSE was ascertained (Figure 9).

As detailed in Section 3.6, the correlation between MW EYE and MW TEYE was nearly identical in these TC cloud patterns, but on the basis of the 10 candidate values for maximum wind speed, the sixth maximum wind speed value (V6) of MW TEYE had a higher correlation than any of the maximum wind speed values for the MW EYE patterns. Conversely, the second and seventh had lower correlations than any maximum wind speed value. Additionally, MW SHEAR and MW BAND showed low correlations for the sixth maximum wind speed value, while the RMSE was high. A difference is thus seen in the regression formula that shows the maximum wind speed with a high correlation to known data according to the analysis pattern. For BT_WP_Ave, the correlation is the highest with MW EYE and MW TEYE, followed by MW SHEAR, while that for MW BAND is low.

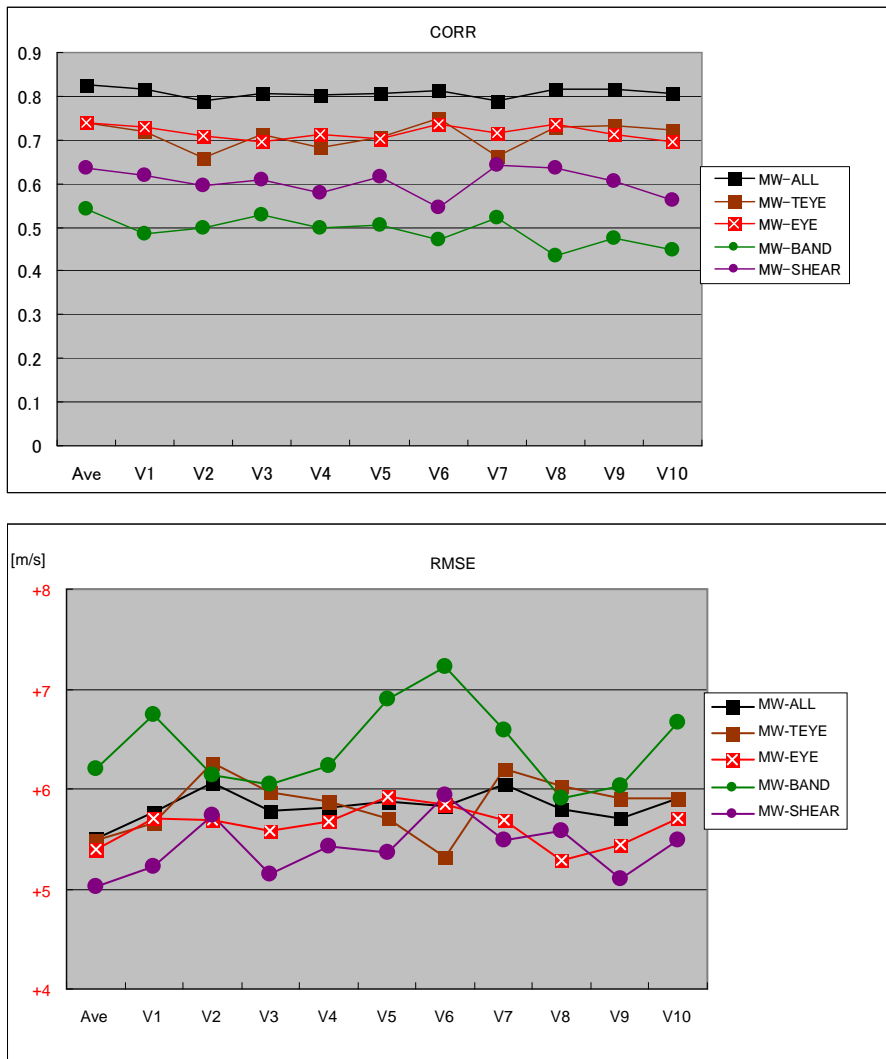
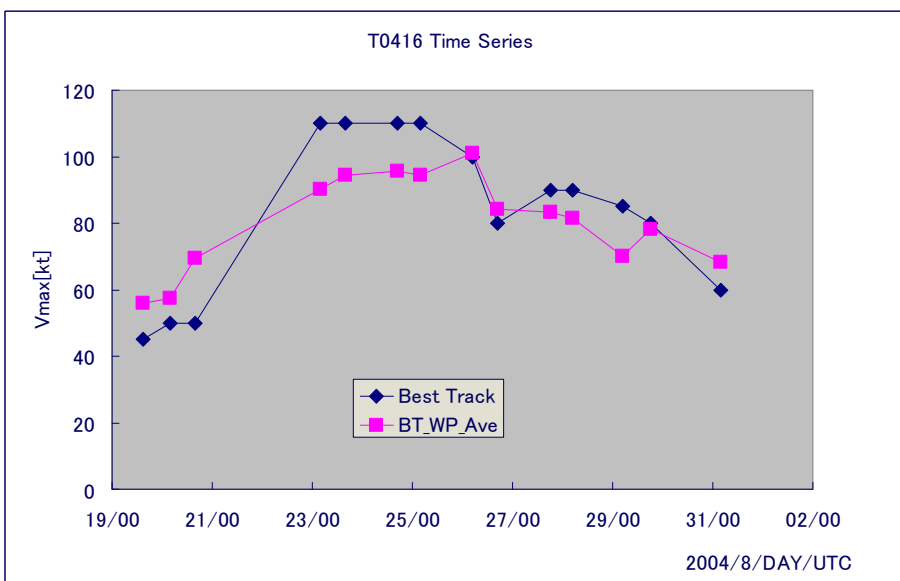
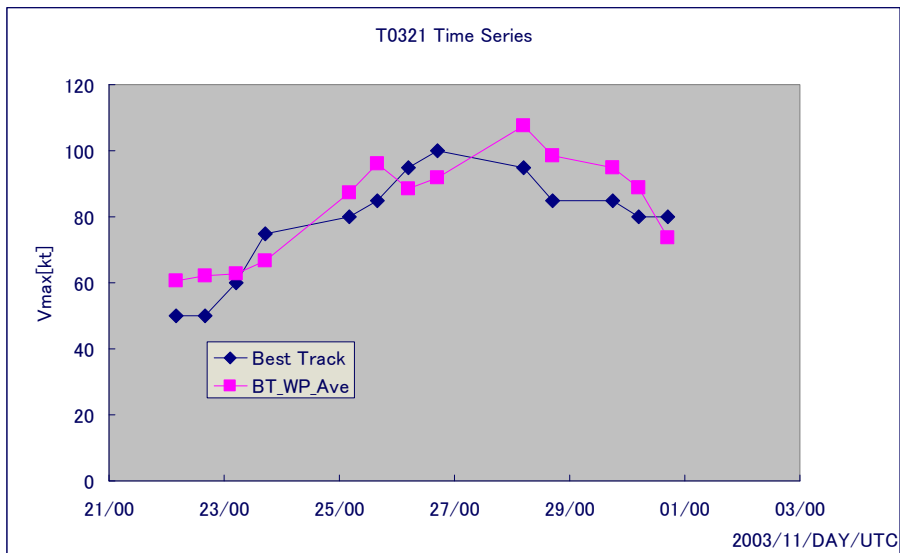


Figure 9 Correlation between best track maximum wind speed and candidate values for the respective maximum wind speeds of BT_WP (top) and RMSE (bottom) (ALL in the figure indicates all patterns. V1 to V10 are the candidate values for the maximum wind speed [Vmax], and Ave is their average.)

3.8 Comparison of time changes in maximum wind speed

An example of checked time changes for the best track maximum wind speed and BT_WP_Ave is shown in Figure 10. Time not captured in Aqua/AMSR-E images cannot be compared and only a part of whole TC life stages can be seen, but on the whole, BT_WP_Ave is calculated as stronger in the early stages of development as compared with the best track maximum wind speed. The calculated increase in wind speed is moderate, however, and toward the mature stage, the results adversely tend to be slightly weaker as compared with the best track maximum wind speed. On the other hand, BT_WP_Ave is calculated with good correspondence in the weakening stage when the best track maximum wind speed weakens, in a similar fashion to the results outlined in 3.7. While

there is a margin of error in the strength from the beginning of the developing stage toward the mature stage, the trend of change shows good correspondence.



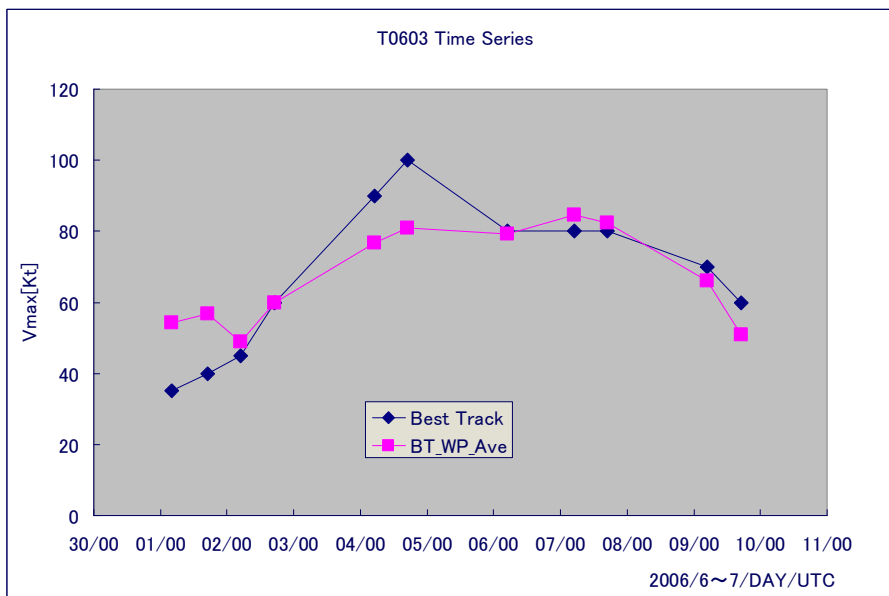
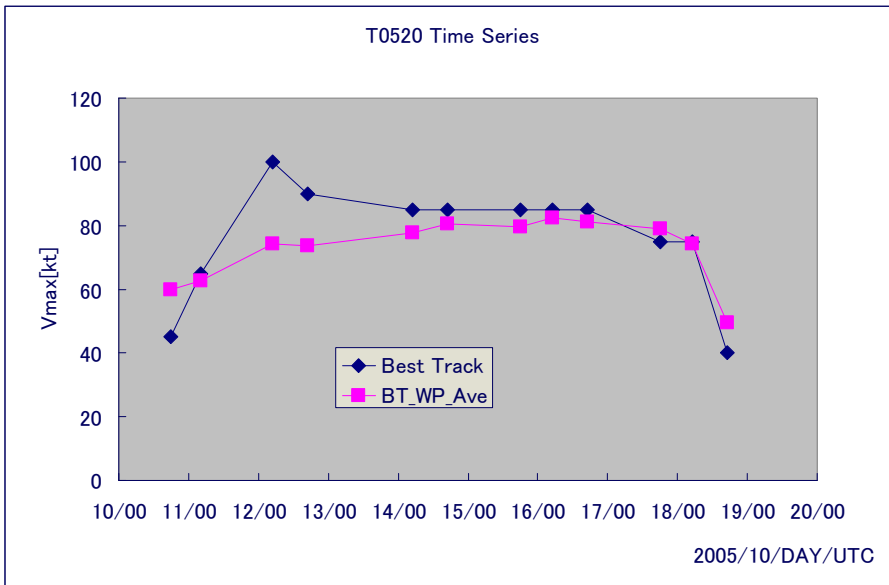


Figure 10 Comparison of time changes between best track maximum wind speed and BT_WP_Ave (from the top: T0321, T0416, T0520 and T0603)

3.9 Comparison of each best track maximum wind speed with BT_WP_Ave

As can be seen from Figure 10, at the beginning of the developing stage, BT_WP_Ave is calculated as stronger than the best track maximum wind speed, but from around 60 KT to 80 KT, the best track maximum wind speed tends to be stronger. Referring to this tendency, statistical research was conducted using the classes of best track maximum wind speed shown in Table 5.

The RMSE is at its smallest when the best track maximum wind speed is from 70 to 79 KT. A large RMSE is seen up to 49 KT and from 90 to 110 KT, and a high positive bias is seen up to 49 KT with a high negative bias from 90 to 110 KT. Additionally, a reversal of positive and negative figures in the average margin of error takes place with a boundary of around 70 KT, indicating that best track maximum wind speeds stronger than this tend to yield a negative bias. This matches the comparison by life stage in Section 3.6 and the results of time change comparison in Section 3.8.

Table 5 Comparison of BT_WP_Ave accuracy by class of best track maximum wind speed

	No. of cases	Average of best track maximum wind speed (KT)	Average of BT_WP_Ave (KT)	Average margin of error (m/s)	RMSE (KT)	RMSE (m/s)
ALL_DATA	470	66.77	67.61	0.43	10.78	5.55
Up to 49 KT	95	41.00	51.92	5.62	13.40	6.89
50 – 59 KT	83	52.35	55.86	1.80	9.23	4.75
60 – 69 KT	62	62.42	63.48	0.55	9.01	4.64
70 – 79 KT	67	72.76	71.50	-0.65	8.57	4.41
80 – 89 KT	90	82.72	79.95	-1.42	8.71	4.48
90 – 110 KT	73	95.21	86.08	-4.70	13.70	7.05

3.10 Effect of rapid TC development or weakening on BT_WP_Ave

As mentioned in Section 2.2, the observation time difference between Aqua/AMSR-E imagery and the best track is three hours at most. Verification was performed to ascertain whether this time difference would have an effect in cases of rapid TC development or weakening. The correlation was checked with the exclusion of any values observed during periods when the change in the MET Number (Model Expected T Number) in the past 24 hours was ± 1.5 as analyzed by the Dvorak method (Table 6). The MET Number is an index used in the Dvorak method to show the present strength of a TC by comparing a current image of it with one from 24 hours earlier and judging the related development or weakening. For the amount of change in the past 24 hours, 1.0 is added (deducted) in the case of standard development (weakening), and 1.5 is added (deducted) in the case of rapid (slow) development. That is, if the amount of change in the MET Number in the past 24 hours is +1.5, the TC is rapidly developing, while a value of -1.5 represents rapid weakening.

The results show that the correlation coefficient became slightly higher (to 0.85 from 0.83 in the overall data), and that the RMSE also improved slightly (to 5.41 m/s from 5.55 m/s in the overall data).

Table 6 Comparison of BT_WP_Ave accuracy upon rapid development/weakening in terms of MET Number change in the past 24 hours

	No. of cases	Average of best track maximum wind speed (KT)	Average of BT_WP_Ave (KT)	Correlation	Average margin of error (m/s)	RMSE (KT)	RMSE (m/s)
ALL_DATA	470	66.77	67.61	0.83	0.43	10.78	5.55
Excluding the MET Number change in the past 24 hours = ± 1.5	361	66.87	68.42	0.85	0.80	10.52	5.41

3.11 Cases with large errors

The difference between the best track maximum wind speed and BT_WP_Ave was ascertained, and cases with a large difference (i.e., a bias of ± 20 KT or more) are shown in Table 7.

Hoshino and Nakazawa (2007) used parameters of high correlation with the best track maximum wind speed and selected 10 regression formulas for small RMSEs from among many parameter combinations. It is therefore not easy to explain the cause of higher bias from formulas created by combinations of various parameters. Consequently, in the frequency band where images can be displayed with the GMSLPM/SATAID analytical tool, comparison was made of images with the parameters used frequently in the regression formula for calculating the 10 candidate values for maximum wind speed shown in Table 1-1, and their characteristics were verified.

The characteristics checked were distribution of brightness temperature (TBB) for images of 7 GHz_H, 7 GHz_V, 10 GHz_H, 19 GHz_H, 19 GHz_V, 24 GHz_H and 89 GHz_V (where V is a vertically polarized wave element and H is a horizontally polarized wave element). The results showed a clear tendency for the brightness temperature distribution of 7 GHz_H. TB07H_AREA110_C10 (the ratio of pixels for which the brightness temperature in a concentric circle with a one-degree radius from the center is 110K or more on the horizontally polarized wave of the 7 GHz band channel) is used most as a parameter, and the cause of the higher bias was verified in the two separate cases of higher positive bias and higher negative bias using the pixel ratio of 110 K or more adopted as a threshold value for this parameter.

(1) Higher positive bias

In Table 7, 17 incidences of BT_WP_Ave being calculated as more than the best track maximum wind speed by 20 KT or more (a higher positive bias) are listed, and 16 out of 17 cases appear in the developing stage when the best track maximum wind speed is 55KT or less. It should also be noted that cases of MW EYE, MW TEYE or MW BAND in the TC cloud patterns of microwave images and Curved Band or Cb Cluster in those of the Dvorak method account for more than 80% (15 out of 17 cases), and BT_WP_Ave may be calculated as higher in these cases.

Here, narrowing down further to the case of a best track maximum wind speed of 55 KT or less in the developing stage, MW TEYE or MW EYE in the TC cloud patterns of microwave images, and Curved Band or Cb Cluster in those of the Dvorak method, the corresponding figure was

found to be 8 out of 17 cases (almost half). To facilitate comparison with higher positive bias cases, a comparison was made with 9 cases of lower bias (i.e., biases of ± 5.0 KT or less were extracted) under the same conditions as these 8 cases.

AREA110_C10 (the ratio of pixels for which the brightness temperature in a concentric circle with a radius of one degree from the center is 110K or more) for incidences of higher positive bias (8 cases) was 50 to 94%, with an average of 74%. On the other hand, the same value for incidences with a smaller margin of error (9 cases) was 13 to 52%, with an average of 36% (Tables 8 and 9).

Images of higher positive bias cases are shown in Figure 11. In all incidences of higher positive bias, AREA110_C10 (the colored parts in the figures) covers nearly half of the one-degree circle at a minimum. On the other hand, in the cases of lower positive bias shown in Figure 12, AREA110_C10 is smaller – about half the size seen in Figure 11.

(2) Higher negative bias

In the cases of Table 7 where BT_WP_Ave is calculated as less than the best track maximum wind speed by 20 KT or more (a higher negative bias), MW EYE or MW TEYE in the TC cloud patterns of the microwave images and Eye in those of the Dvorak method account for most incidences (9 out of 11). Additionally, all appear in the mature stage and have the characteristic of a higher best track maximum wind speed in contrast to cases with a higher positive bias.

The top 10 cases of higher negative bias for AREA110_C10 (the ratio of pixels for which the brightness temperature in a concentric circle with a radius of one degree from the center is 110 K or more) are shown in Table 10. The top 10 cases of lower bias (either positive or negative) are shown in Table 11 among the cases with best track maximum wind speeds of 90 KT or more, because most of the cases of higher negative bias (shown in Table 10) were found when best track maximum wind speeds were 90 KT or more (MW TEYE in the TC cloud patterns of microwave images).

Figure 13 shows images of cases where the BT_WP_Ave wind speed was lower (a higher negative bias) than the best track maximum wind speed, and Figure 14 shows images of cases with a lower bias. In all cases of higher negative bias, AREA110_C10 does not fully cover the concentric circle with a one-degree radius (90% or less). On the other hand, it fully covers the circle in all cases of lower bias. AREA110_C10 shows an average of 65% (36 to 90%) for 10 cases of higher negative bias, and 100% (fully covering a concentric circle with a radius of one degree from the center) for all 10 cases of lower bias.

A trend is also seen (as shown in Figure 15) whereby smaller AREA110_C10 values are accompanied by lower BT_WP_Ave wind speed estimation, thereby making the negative bias higher.

Table 7 Cases of higher bias; large differences between best track maximum wind speed and BT_WP_Ave (bias of ± 20 KT or more)

YYYY/MM/DD Time	Best track maximum wind speed [KT]	BT_WP_ Ave [KT]	Error [KT]	MW cloud pattern	Dvorak method cloud pattern	TC life stage
2004/08/28, 03 UTC	40	68.9	+28.9	TEYE	Curved Band	Developing
2005/10/29, 06 UTC	40	68.3	+28.3	EYE	Curved Band	Developing
2006/08/14, 05 UTC	35	61.7	+26.7	EYE	Cb Cluster	Developing
2003/09/06, 04 UTC	35	60.2	+25.2	BAND	Cb Cluster	Developing
2006/08/08, 18 UTC	40	64.2	+24.2	SHEAR	Curved Band	Developing
2004/06/06, 18 UTC	35	58.9	+23.9	TEYE	Cb Cluster	Developing
2004/11/17, 05 UTC	50	73.5	+23.5	TEYE	Curved Band	Developing
2004/04/05, 04 UTC	40	63.2	+23.2	TEYE	Cb Cluster	Developing
2003/09/06, 16 UTC	40	63.0	+23.0	SHEAR	Cb Cluster	Developing
2006/11/09, 17 UTC	45	67.7	+22.7	TEYE	Curved Band	Developing
2006/08/06, 04 UTC	45	67.4	+22.4	BAND	Cb Cluster	Developing
2004/05/18, 17 UTC	35	57.2	+22.2	BAND	Cb Cluster	Developing
2005/08/23, 16 UTC	55	76.7	+21.7	EYE	Curved Band	Developing
2004/08/08, 17 UTC	45	66.5	+21.5	BAND	Cb Cluster	Developing
2003/08/29, 17 UTC	35	56.3	+21.3	BAND	Curved Band	Developing
2006/08/06, 16 UTC	50	70.8	+20.8	BAND	Curved Band	Developing
2003/08/24, 19 UTC	65	85.2	+20.2	TEYE	B-Eye	Mature
2006/08/08, 18 UTC	90	69.9	-20.1	TEYE	CDO	Mature
2005/09/28, 05 UTC	90	68.6	-21.4	TEYE	Eye	Mature
2005/10/30, 19 UTC	80	58.3	-21.7	EYE	Eye	Mature
2005/06/04, 05 UTC	95	71.5	-23.5	TEYE	Eye	Mature
2005/06/04, 18 UTC	90	65.9	-24.1	EYE	CDO	Mature
2005/10/12, 05 UTC	100	74.4	-25.6	TEYE	Eye	Mature
2005/06/03, 05 UTC	90	64.1	-25.9	TEYE	Eye	Mature
2004/10/07, 18 UTC	100	71.0	-29.0	TEYE	Eye	Mature
2004/10/08, 05 UTC	100	69.2	-30.8	TEYE	Eye	Mature
2006/11/10, 17 UTC	95	61.7	-33.3	TEYE	Eye	Mature
2006/11/10, 06 UTC	90	55.3	-34.7	TEYE	Eye	Mature

Table 8 Cases of higher positive bias; lower BT_WP_Ave wind speed than the best track maximum wind speed (MW EYE or MW Band in the TC cloud patterns of microwave images and Curved Band or Cb Cluster in those of the Dvorak method)

Error [KT]	Best track maximum wind speed [KT]	BT_WP_Ave [KT]	TB07H_AREA110_C10 [%]
+28.9	40	68.9	88
+28.3	40	68.3	71
+26.7	35	61.7	64
+23.9	35	58.9	50
+23.5	50	73.5	83
+23.2	40	63.2	72
+22.7	45	67.7	73
+21.7	55	76.7	94
Ave. +24.8	Ave. 43	Ave. 67.0	Ave. 74

Table 9 Cases of lower bias; smaller differences between the best track maximum wind speed and the BT_WP_Ave wind speed (MW EYE or MW BAND in the TC cloud patterns of microwave images and Curved Band or Cb Cluster in those of the Dvorak method)

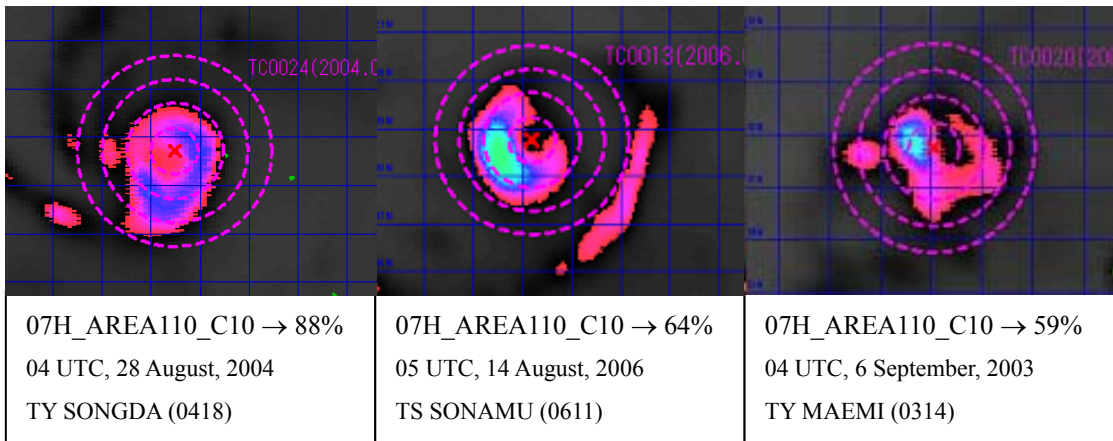
Error [KT]	Best track maximum wind speed [KT]	BT_WP_Ave [KT]	TB07H_AREA110_C10 [%]
+1.8	50	51.8	28
+2.0	50	52.0	43
+2.5	50	52.5	33
+3.4	50	53.4	42
-1.8	55	53.2	52
-1.4	55	53.6	42
-0.8	55	54.2	13
+1.9	55	56.9	31
+2.7	55	57.7	40
Ave. +1.1	Ave. 53	Ave. 54.0	Ave. 36

Table 10 Cases of higher negative bias; lower BT_WP_Ave wind speed than the best track maximum wind speed

Error [KT]	Best track maximum wind speed [KT]	BT_WP_Ave [KT]	TB07H_AREA110_C10 [%]
-34.7	90	55.3	36
-33.3	95	61.7	60
-30.8	100	69.2	66
-29.0	100	71.0	70
-25.9	90	64.1	56
-25.6	100	74.4	90
-24.1	90	65.9	68
-23.5	95	71.5	74
-21.7	80	58.3	55
-21.4	90	68.6	80
Ave. -27.0	Ave. 93	Ave. 66.0	Ave. 65

Table 11 Cases of lower bias; smaller difference between the best track maximum wind speed and the BT_WP_Ave wind speed (best track maximum wind speed of 90 KT or more)

Error [KT]	Best track maximum wind speed [KT]	BT_WP_Ave [KT]	TB07H_AREA110_C10 [%]
+1.6	90	91.6	100
+1.2	100	101.2	100
+0.6	90	90.6	100
+0.4	90	90.4	100
+0.2	90	90.2	100
-0.1	95	94.9	100
-0.7	90	89.3	100
-1.2	90	88.8	100
-1.3	90	88.7	100
-1.4	95	93.6	100
Ave. -0.1	Ave. 92	Ave. 91.9	Ave. 100



[Brightness temperature gradation] (values of less than 110K are indicated in grayscale)

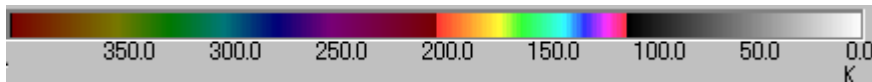


Figure 11 Sample images of a horizontally polarized wave on the 7 GHz band channel in the case of the higher positive bias shown in Table 8 (The dashed lines are concentric circles with radii increasing in increments of 0.5 degrees from the center. The area of the concentric circle with a radius of 1 degree from the center is C10. Colored areas indicate brightness temperatures of 110 K or more.)

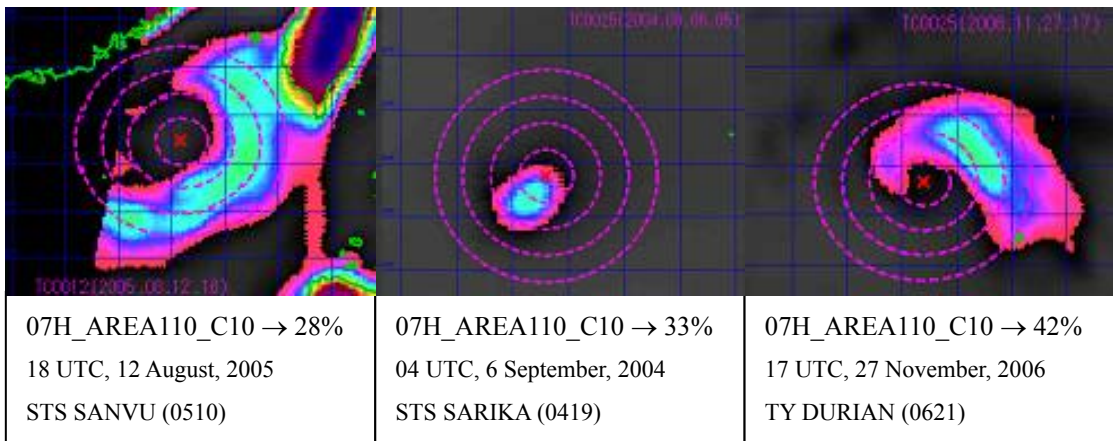


Figure 12 Sample images of a horizontally polarized wave on the 7 GHz band channel in the case of the lower bias shown in Table 9 (display elements and color scale as per those for Figure 11)

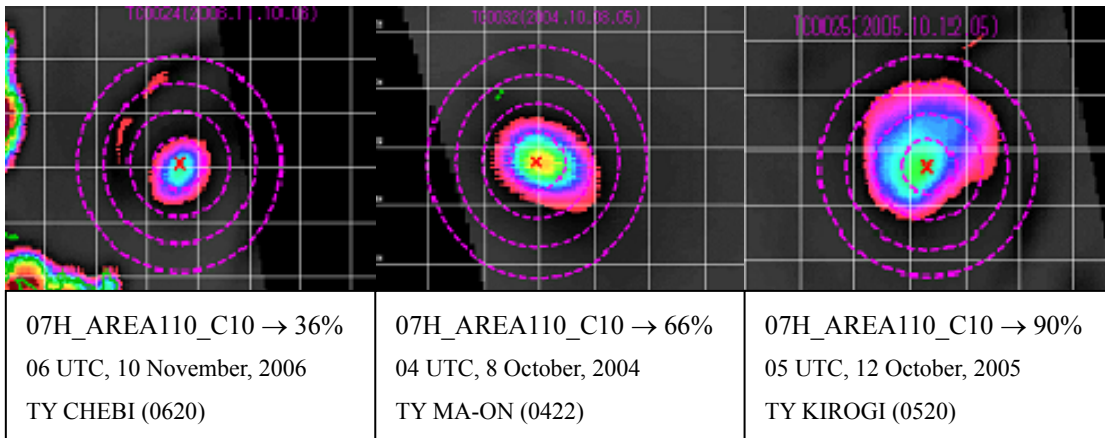


Figure 13 Sample images of a horizontally polarized wave on the 7 GHz band channel in the case of the higher negative bias shown in Table 10 (display elements and color scale as per those for Figure 11)

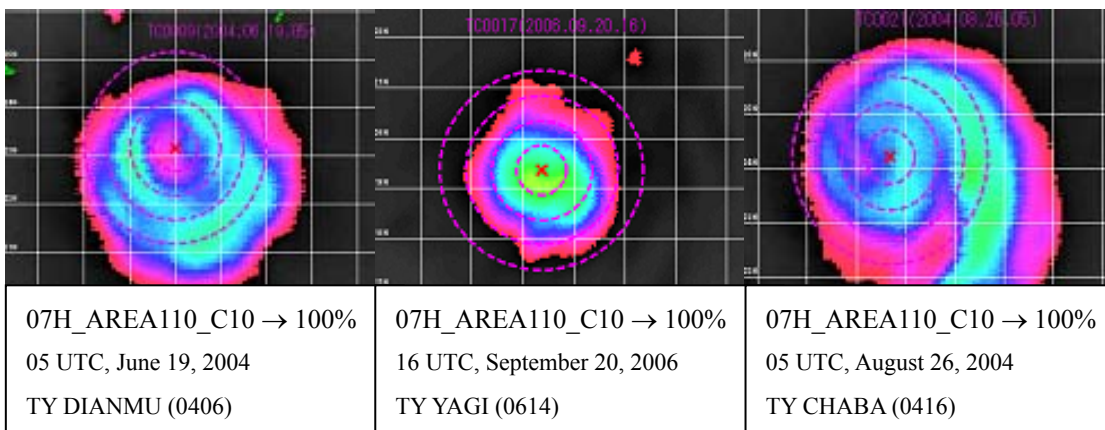


Figure 14 Sample images of a horizontally polarized wave on the 7 GHz band channel in the case of the lower bias shown in Table 11 (display elements and color scale as per those for Figure 11)

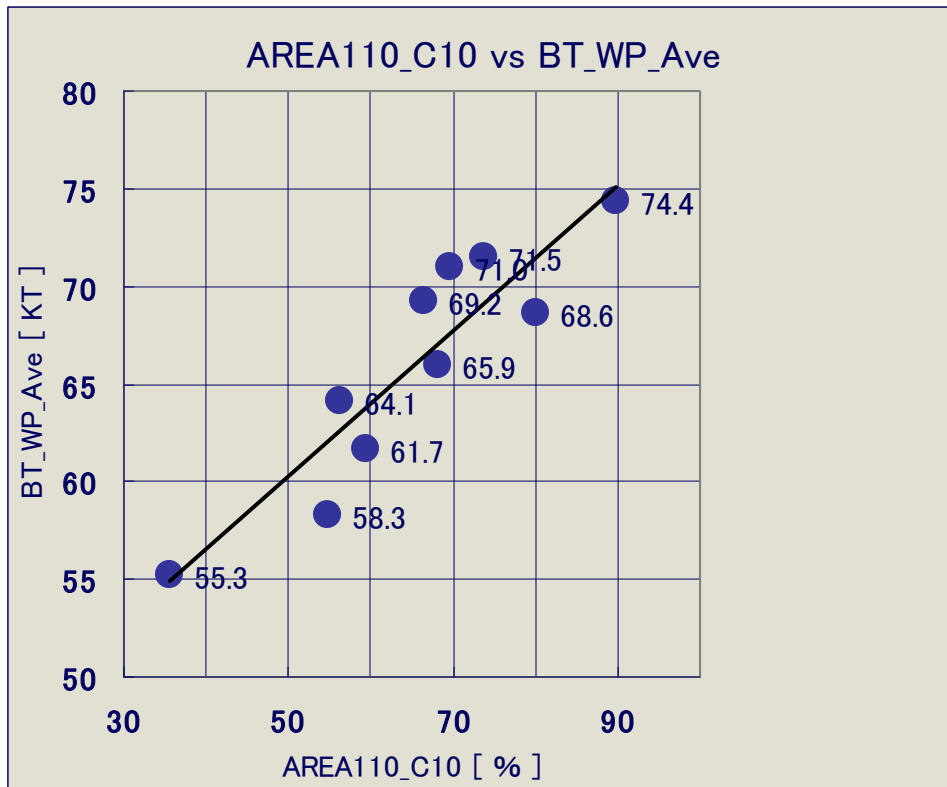


Figure 15 Scatter diagram of AREA110_C10 (horizontally polarized wave on the 7 GHz band channel) and BT_WP_Ave (figures in the graph are BT_WP_Ave [KT])
The straight line in the figure is the regression line.

3.12 Summary of verification results

The verification results obtained from this research are summarized below. (The results pertain to BT_WP_Ave [data from 2003 to 2006], thereby eliminating the effect of land.)

- (1) The correlation coefficient between the best track maximum wind speed and BT_WP_Ave was high at 0.83. This was the same as the trend seen in verification by year, and a similarly high correlation was observed irrespective of whether the data were subordinate or independent.
- (2) The results of accuracy verification for the best track maximum wind speed and BT_WP_Ave from various perspectives are outlined below.
 - (i) Comparison by TC life stage (developing, mature and weakening) showed that BT_WP_Ave is calculated as stronger than the best track maximum wind speed in the developing stage, and that many of the cloud patterns of the Dvorak method are Cb Cluster or Curved Band. In the mature stage, the best track maximum wind speed and BT_WP_Ave correspond closely, but in the cases of the Eye pattern of the Dvorak method, BT_WP_Ave may be calculated weaker than the best track maximum wind speed. In the weakening stage, the level of error tends to be smaller than in the development or mature stages, and Shear or Curved Band is mostly seen in terms of the cloud patterns of the Dvorak method.

- (ii) In comparison by TC cloud patterns for microwave images, BT_WP_Ave showed the highest correlation in MW EYE or MW TEYE, followed by MW SHEAR. MW BAND gives the lowest correlation.
- (iii) As outlined in Section 3.10, BT_WP_Ave tends to show a worse correlation when the TC is either rapidly developing or rapidly weakening.
- (iv)-(1) A case in which the calculated BT_WP_Ave value showed a high positive bias (calculated as at least 20 KT higher) appeared in the developing stage when the best track maximum wind speed was 55 KT or less, and cases of MW EYE, MW TEYE or MW BAND in the TC cloud patterns of microwave images and Curved Band or Cb Cluster in those of the Dvorak method accounted for more than 80% of the total. About half the cases of higher positive bias were found when the best track maximum wind speed was 55 KT or less in the developing stage and in cases of MW TEYE or MW EYE in the TC cloud patterns of microwave images and Curved Band or Cb Cluster pattern in those of the Dvorak method. When compared with cases of lower bias (with biases of ± 5.0 KT or less extracted) under the same conditions, AREA110_C10 of all higher positive bias cases generally covered more than half of the one-degree circle. On the other hand, its size in lower positive bias cases was reduced to about half that seen in higher positive bias cases.
- (iv)-(2) Of the cases in which the calculated BT_WP_Ave showed a high negative bias (calculated as at least 20 KT lower), MW EYE or MW TEYE in the TC cloud patterns of microwave images and Eye in those of the Dvorak method accounted for the majority (9 cases out of 11), all appeared in the mature stage with the characteristic of a higher best track maximum wind speed than the higher positive bias cases of (iv)-(1), and the best track maximum wind speed was 90 KT or more in 10 out of 11 higher negative bias cases. Comparison with 10 lower bias cases in incidences of a best track maximum wind speed of 90 KT or more showed that all the lower bias cases had 100% AREA110_C10 coverage, whereas in all the higher negative bias cases, AREA110_C10 did not fully cover the one-degree concentric circle, with an average coverage of 65%. Additionally, the wind speed of BT_WP_Ave was estimated as lower for smaller AREA110_C10 sizes, thus highlighting the trend of higher negative bias.

4. Consideration

- (1) In accuracy verification by TC cloud patterns of microwave images, the causes for the lowest correlation of MW BAND were reviewed. As seen from Table 12, if the TC cloud pattern of microwave imagery is MW BAND, the emergence frequency of Curved Band or Cb Cluster in those of the Dvorak method approaches 70%. As seen from Table 4, Curved Band or Cb Cluster in the cloud patterns of the Dvorak method is likely to appear in the generating stage or the developing stage, and has no eye or low-level cloud vortex to clearly suggest the location of the center. Determining the center position in such cases lacks accuracy because it is taken as the center of the curvature factor or the emergence point of convective cloud lines pointing to the center, which can be considered multiple. This is seen as one of the reasons for the lower level of accuracy in determining the center position and for the higher level of error as compared to other

TC cloud patterns of microwave images. Additionally, the presence of convective clouds near the center even without strong winds could make the calculated BT_WP value higher and increase the level of error.

The frequent appearance of MW BAND in the TC cloud patterns of microwave images in the generating stage or the developing stage and the higher calculated BT_WP value correspond to the verification result showing that BT_WP_Ave is calculated as stronger when the best track maximum wind speed is low (in the generating or developing stages of the Dvorak method).

- (2) As better accuracy is seen in the TC weakening stage, analysis results with a higher level of objectivity can be obtained by referring to BT_WP_Ave when TC cloud patterns of the Dvorak method are not clear in the weakening stage.
- (3) The verification result of BT_WP_Ave showing a high positive bias (calculated as at least 20 KT higher than the best track value) or a high negative bias (calculated as at least 20 KT lower than the best track value) indicates that TB07H_AREA110_C10 (the ratio of pixels for which the brightness temperature in a concentric circle with a one-degree radius from the center is 110K or more on the horizontally polarized wave of the 7 GHz band channel) can be used for effective judgment in cases with large errors.

To calculate the 10 candidate values for maximum wind speed, various combinations of parameters are used to create a regression formula. Although it is difficult to determine the cause of the significant divergence from TB07H_AREA110_C10 only, a judgment factor can be obtained.

- (4) Usage in actual operation is considered from the verification results. As analytical results according to the Dvorak method are generally relied on in typhoon intensity analysis, the flowchart in Figure 16 was prepared using the relationship between the Dvorak method CI number and the maximum wind speed (as shown in Table 13) as well as by considering the TC life stage. As mentioned earlier, the CI number of the Dvorak method is equivalent to the T number in the TC generating and developing stages.

As seen from the above, TC intensity estimation with a higher level of accuracy can be expected by adding intensity estimation from microwave imagery to intensity analysis using the conventional Dvorak method.

Table 12 Emergence frequency of visible and infrared (IRVIS) cloud patterns and microwave (MW) analytical cloud patterns in the Dvorak method (from Nishimura et al. [2007])
(MW EYE includes the MW TEYE instances in this research.)

	IRVIS Curved Band	IRVIS Banding Eye	IRVIS Embedded	IRVIS Eye	IRVIS Shear	IRVIS Cb-Cluster
MW SHEAR	3.5	4.8	0.0	0.0	71.4	22.7
MW EYE	64.9	95.2	100.0	100.0	14.3	40.9
MW BAND	31.6	0.0	0.0	0.0	14.3	36.4

(%)

Table 13 Relationship between the Dvorak method CI number and maximum wind speed in the western North Pacific (Koba et al. [1990])

CI number	Maximum wind speed (KT)
1.0	22
1.5	29
2.0	36
2.5	43
3.0	50
3.5	57
4.0	64
4.5	71
5.0	78
5.5	85
6.0	93
6.5	100
7.0	107
7.5	115
8.0	122

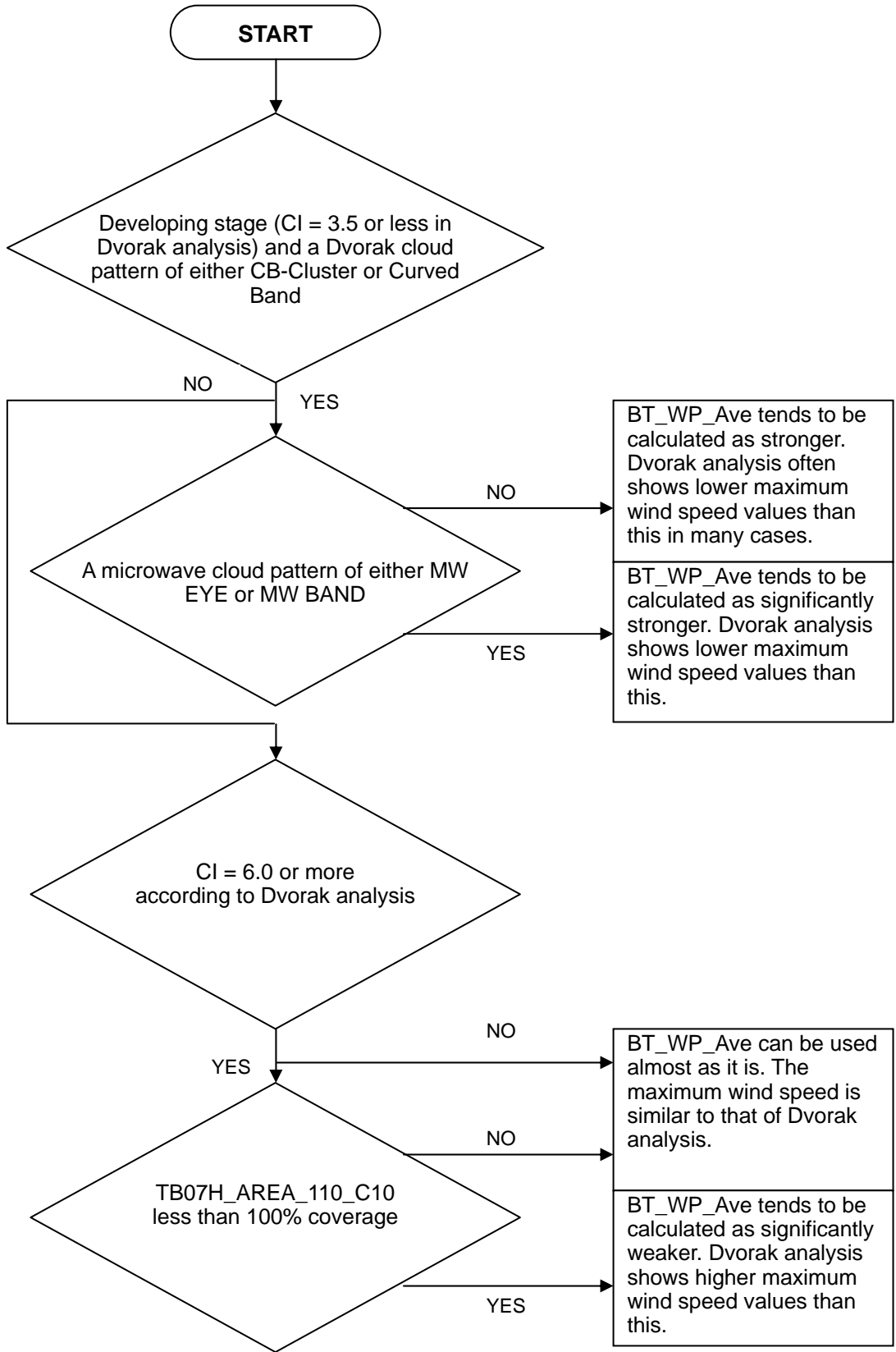


Figure 16 Flowchart for operational use

5. Conclusion

Using the Aqua/AMSR-E version of TC intensity estimation according to the technique of Hoshino and Nakazawa (2007), comparison was made between the average of 10 candidate values for maximum wind speed and the best track maximum wind speed value. The results indicated that independent data showed a high correlation similar to that of subordinate data.

From the perspective of TC life, in the developing stage (corresponding to the stages of generating to developing in the Dvorak method), BT_WP_Ave tends to be calculated as stronger than the best track maximum wind speed, and Cb Cluster or Curved Band in the cloud patterns of the Dvorak method often appears. Furthermore, in cases where the TC cloud patterns of microwave images were MW EYE, MW TEYE or MW BAND, BT_WP_Ave was calculated as significantly stronger. In the mature stage, the RMSE and average error became smaller and corresponded more closely to the best track, but BT_WP_Ave was calculated as weaker when the TC cloud pattern of microwave images was MW EYE or MW TEYE. For this reason, negative bias tended to be significantly larger for TCs with a maximum wind speed exceeding 90 KT. Ascertaining whether TB07H_AREA110_C10 fully covers the one-degree circle or not is effective as a judgment factor to confirm whether such cases of negative bias are particularly significant. If it does not cover the circle, there is a high chance of a significant negative bias. In the weakening stage, Shear or Curved Band in the cloud patterns of the Dvorak method often appears, and largely similar values to those of the best track are often calculated. It can therefore be concluded that analysis results with a higher level of objectivity are obtained by referring to BT_WP_Ave when TC cloud patterns of the Dvorak method are not clear for periods considered to be in the weakening stage.

From the above results, a flowchart for TC intensity estimation using the Dvorak method and microwave imagery was devised.

TC intensity estimation using the technique of Hoshino and Nakazawa (2007) can be considered to complement TC intensity analysis using the Dvorak method and enable higher levels of accuracy and objectivity.

Bibliography

- Dvorak, V. F., 1975: Tropical cyclone intensity analysis and forecasting from satellite imagery, *Mon. Wea. Rev.*, 103, 420 – 430
- Dvorak, V. F., 1984: Tropical cyclone intensity analysis using satellite data, NOAA Technical Report NESDIS 11, p. 47
- Kumabe, R., 2000: CAL development in Meteorological Satellite Center, *Geophysical Magazine*, 3, 109 – 121
- Shunsuke Hoshino, Tetsuo Nakazawa, 2007: Estimation of Tropical Cyclone's Intensity Using TRMM/TMI Brightness Temperature Data, *Journal of the Meteorological Society of Japan*, Vol. 85, No. 4, pp. 437 – 454, Meteorological Society of Japan
- Meteorological Satellite Center, 1999: CAL development at the Meteorological Satellite Center, *Meteorology Journal*, 66.2, 43 – 50
- Meteorological Satellite Center, 2004: Analysis and use of meteorological satellite images: Tropical cyclones, Meteorological Satellite Center, 50 – 63, 72 – 87
- Ryoji Kumabe, 2001: Meteorological Society of Japan Autumn 2000 Symposium, Atmospheric observation from satellites: Historical development, 26 – 30
- Hiroyuki Koba, Takeshi Hagiwara, Shingo Osano, Shuhei Akashi, 1990: Relationship between CI number from Dvorak's technique and minimum sea level pressure or maximum wind speed of Tropical Cyclone, *Research Journal*, 42 (2), 59 – 67
- Shuji Nishimura, Shiro Yoshida, Takeshi Endo, Kohei Otsubo, Koki Mori, Sadao Saito, Koji Kato, Ryo Oyama, Akihiro Shimizu, Junichi Asano, 2007: Analysis of tropical cyclones with microwave satellite imagery, Meteorological Satellite Center Technical Note No. 49, Meteorological Satellite Center, 91 – 125

Quantitative Precipitation Estimation and Quantitative Precipitation Forecasting by the Japan Meteorological Agency

Kazuhiko NAGATA

Forecast Division, Forecast Department

Japan Meteorological Agency

1. Introduction

Typhoons sometimes hit countries in East Asia and Southeast Asia, and may bring various hazards including sediment-related disasters, flooding and inundation. To prevent and mitigate damage from such disasters, analysis and forecasting of precipitation amounts is very important. Analysis relating to the distribution of rainfall amounts is called Quantitative Precipitation Estimation (QPE), and that relating to forecasting is called Quantitative Precipitation Forecasting (QPF). The Japan Meteorological Agency (JMA) developed QPE and QPF products as well as QPE/QPF-induced products using radar data, rain gauge data and numerical weather prediction (NWP) output. Figure 1 shows the relationships that link these various data and products, including QPE and QPF.

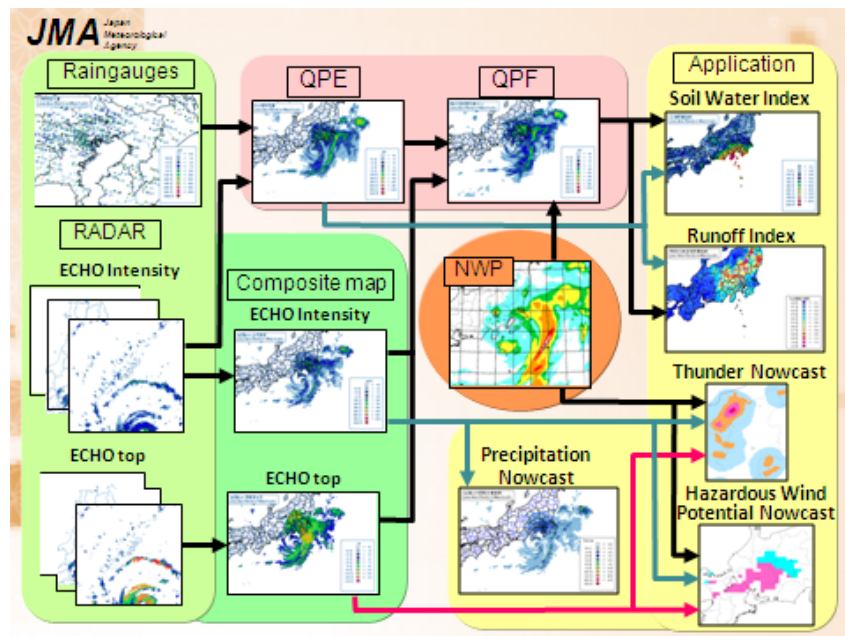


Fig. 1 Various precipitation products derived from rain gauge and radar data

2. Radar/Rain gauge-Analyzed Precipitation

Radar/Rain gauge-Analyzed Precipitation (referred to here as “R/A”) is a QPE product of JMA. It shows one-hour cumulative rainfall with a spatial resolution of 1 km, and is issued every 30 minutes. Figure 2 shows a sample.

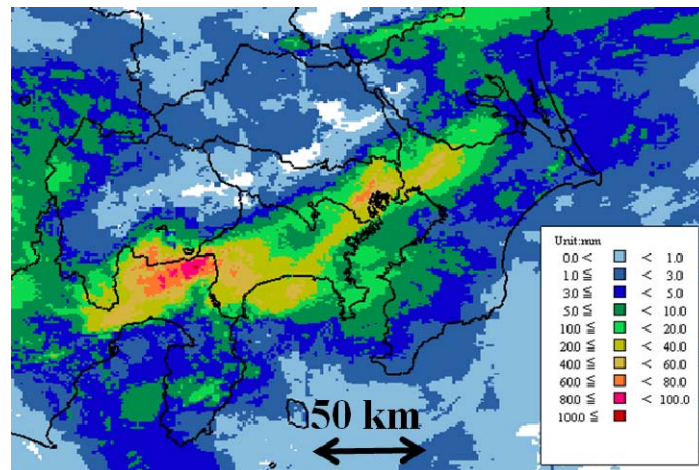


Fig. 2 Sample of R/A product (06 UTC, 8 Sep. 2010)

2.1 Observation data used to produce R/A

Both rain gauge and radar data are used to produce R/A. Although rain gauges measure precipitation amounts with satisfactory accuracy, they can observe only at a single point. Conversely, radars can observe large areas at the same time with a higher spatial resolution than the rain gauge network, but may produce readings different from those obtained with a ground-based rain gauge as they measure amounts of rain overhead. Their accuracy is also not as reliable as that of rain gauges because they are remote sensing instruments. For monitoring and prediction of sediment-related disasters, flooding and inundation, the rain gauge network is too rough and radar observation lacks sufficient accuracy. For this reason, JMA produces R/A by calibrating one-hour accumulated radar echo data with one-hour accumulated rain gauge precipitation data. It collects data from 10,000 rain gauges operated by JMA, the Ministry of Land, Infrastructure, Transport and Tourism (MLIT) and local governments every ten minutes or every hour (rain gauges are located in every 7-km grid square on average) and data from 46 C-band radars operated by JMA and MLIT with a spatial resolution of 1 km every five minutes. Each radar covers an area of 500 km × 500 km.

2.2 R/A algorithms

The procedure for producing R/A involves the following three steps:

1. Accumulation of radar intensity data
2. Calibration of radar data
3. Composition of calibrated radar data

This section briefly describes each process.

2.2.1 Accumulation of radar intensity data

First, echo intensity data obtained every five minutes are accumulated. If echoes move too fast, one-hour accumulated echo intensities sometimes show an unnatural striped pattern (see the image on the left of Fig. 3). To avoid such unnatural patterns, accumulation must be conducted taking account of echo movements (see the image on the right of Fig. 3). In this process, the observed echoes are divided into pieces and traced every five minutes. Then, by summing up the echo intensities passing a grid, the one-hour accumulated echo intensity of the grid is estimated. Quality checking of echo intensities is also conducted at this stage.

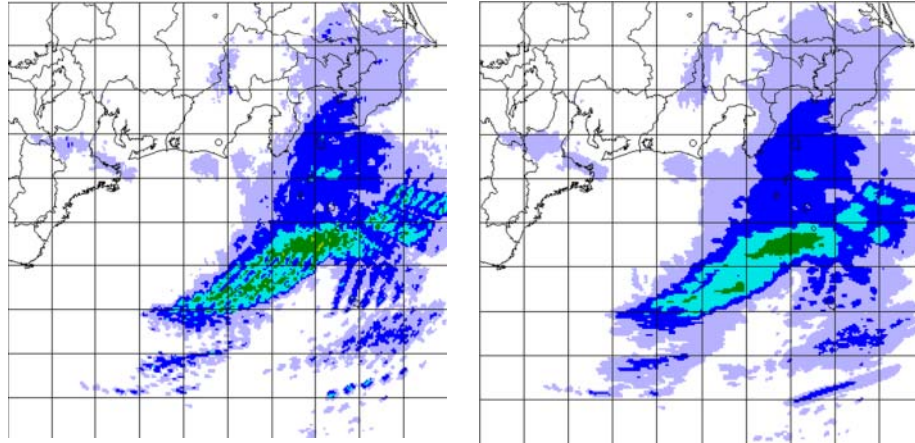


Fig. 3 Accumulation of radar intensity data

Left: one-hour accumulated echoes; right: as per the figure on the left, but with consideration of echo movements

2.2.2 Calibration of radar data

To produce accurate QPE, calibration of one-hour accumulated radar data is performed to fit the distribution of one-hour accumulated rain gauge data. Calibration is conducted in two steps. First, each piece of radar data is calibrated to fit averaged rain gauge data within the relevant observation range. Then, detailed calibration of radar data over land is conducted to fit rain gauge data on local scales.

2.2.2.1 Calibration over the whole radar observation range

Values of one-hour precipitation estimated from the accumulation of radar echo intensities in a certain grid are generally different from observation values from a rain gauge in the grid. As rain gauge measurement is more reliable, the accumulation of radar echo intensities is calibrated with rain gauge observations within the radar observation range to meet the following two conditions:

- (1) The average of the calibrated accumulation for radar echo intensities over a certain domain should be equal to that of all other radars observing the same domain.
- (2) The average of the calibrated accumulation for radar echo intensities over a certain grid should be equal to the average of the rain gauge observations.

Figure 4 shows a sample of this calibration. The figure on the left shows one-hour precipitation estimated

from the accumulation of radar echo intensities; the central figure shows one-hour precipitation after calibration to meet the two conditions outlined above; and the figure on the right shows the one-hour precipitation observed by rain gauges. The original accumulation of radar echo intensities (left) in a certain grid is less than the rain gauge observation in the same grid (right). Due to calibration, the central figure shows more precipitation than that on the left. The figure on the right is closer to the central figure than the left figure.

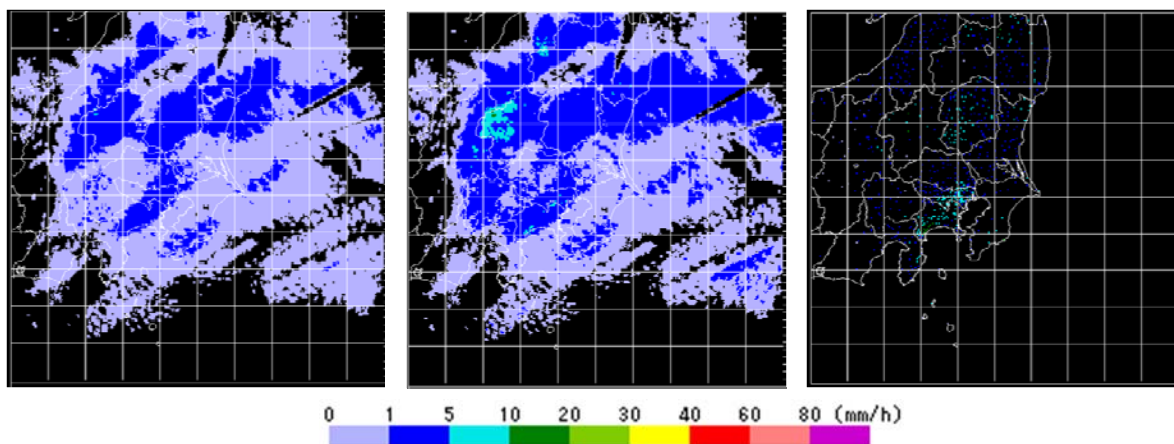


Fig. 4 Left: sample of one-hour precipitation estimated by accumulating echo intensities; center: after calibration; right: from raingauge observations

2.2.2.2 Calibration over land

The calibrated echo intensities explained above are further calibrated to enable expression of more detailed patterns of precipitation on local scales (Makihara, 2000). For example, the calibrated accumulation of echo intensities for a certain grid g derived using the method described in 2.2.2.1 is calibrated again using data from rain gauges within about 40 km of that grid. A calibration factor for grid g is calculated with weighted interpolation of the calibration factors of the surrounding grids that contain rain gauges within 40 km of the grid. Here, the calibration factor for the grid is defined as the ratio of rain gauge observation values to the calibrated accumulation of radar echo intensities in the grid using the method outlined in 2.2.2.1. The following factors are taken into account to calculate the weight of interpolation:

- (1) Distances between grid g and rain gauges
- (2) Differences between echo intensity for grid g and those for grids containing rain gauges
- (3) Beam attenuation rate for precipitation
- (4) Uniformity of rain gauge distribution

Multiplying the calibrated echo intensities by the calibration factor as determined above gives the estimated precipitation for grid g .

Figure 5 shows a sample of this calibration. The figure on the left shows calibrated accumulation of radar

echo intensities calculated using the method outlined in 2.2.2.2, and that on the right shows one-hour rain gauge data (in the same way as the image on the right of Fig. 4). The figure on the left matches the rain gauge data better than the central image in Fig. 4.

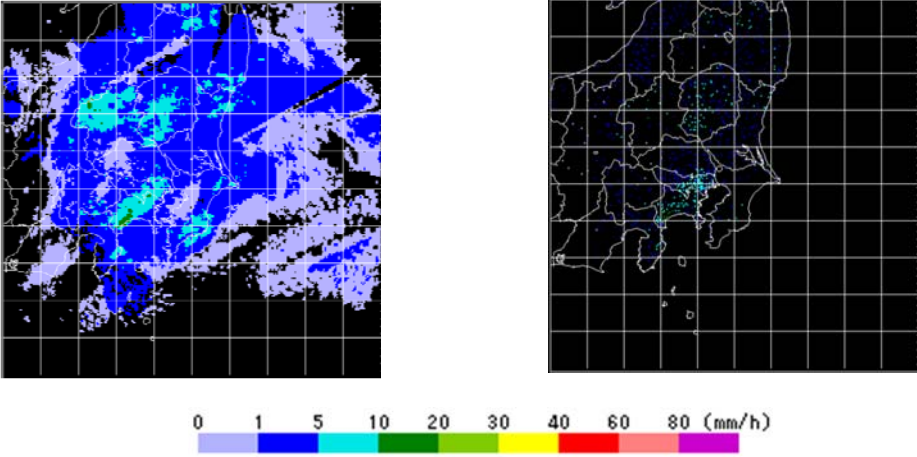


Fig. 5 Left: sample of one-hour precipitation after calibration over land; right: the corresponding raingauge observations (as per the image on the right of Fig. 4)

2.2.3 Composition of calibrated radar data

After the above calibration, a composite precipitation map is produced using the calibrated accumulation of echo intensities calculated using the method outlined in 2.2.2.2 from 46 radars located around the country by transforming the coordination from zenithal projection into latitude-longitude grids with equidistant cylindrical projection. If two or more radars observe the same grid, the greater value is selected. Figure 6 shows calibrated echo intensities covering each region and a composite precipitation map of the country.

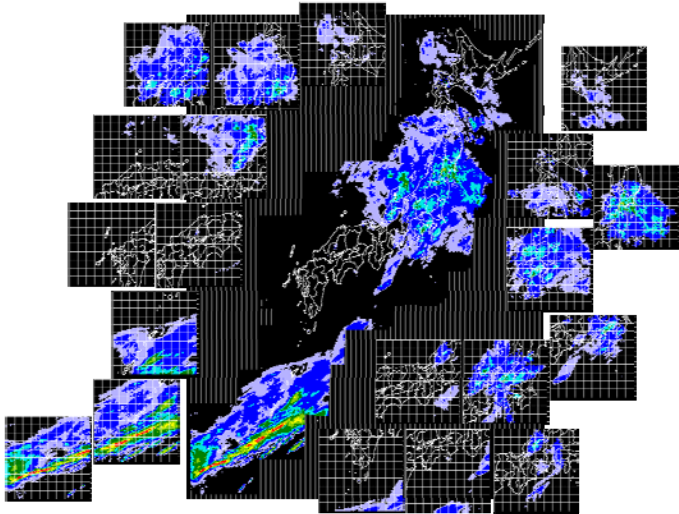


Fig. 6 Radar data covering each region and a composite precipitation map

2.3 Accuracy of R/A

To assess the accuracy of R/A, experimental R/A data for verification excluding rain gauge data at about 200 observing points were prepared, and were compared with the excluded rain gauge data. Rain gauge observation values were compared with R/A values for nine grids (a central grid and the eight grids surrounding it) considering location errors equivalent to the dimensions of one grid (i.e., 1 km) stemming from wind-related advection of raindrops before their arrival at ground level, and/or errors resulting from coordinate transform.

Figure 7 shows a scatter plot comparing hourly R/A values and corresponding rain gauge measurements taken over a period of four months during the warm season (from August to November of 2009). Only the best R/A values out of the nine grids are plotted. The figure shows close agreement between R/A values and rain gauge measurements.

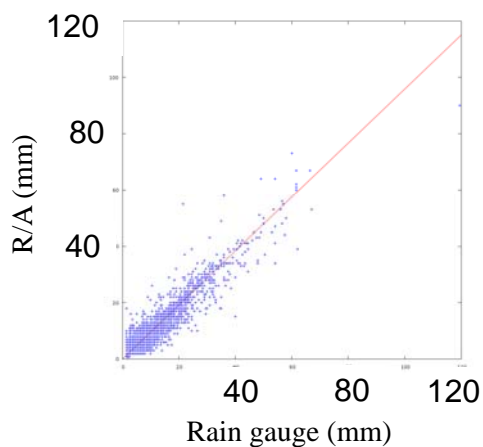


Fig. 7 Scatter plot of R/A and rain gauge data with a regression line (red)
($R/A = 0.96 \times \text{Raingauge}$)

3. Very-short-range Forecasting of Precipitation

Very-short-range Forecasting of Precipitation (referred to here as “VSRF”) is a QPF product of JMA. It provides hourly precipitation forecasting up to six hours ahead with a spatial resolution of 1 km. VSRF is calculated by merging the forecast precipitation with values from JMA’s mesoscale model (MSM) and the extrapolated composite echo intensity. Figure 8 shows a sample of VSRF. An outline of the procedures for producing VSRF is given below.

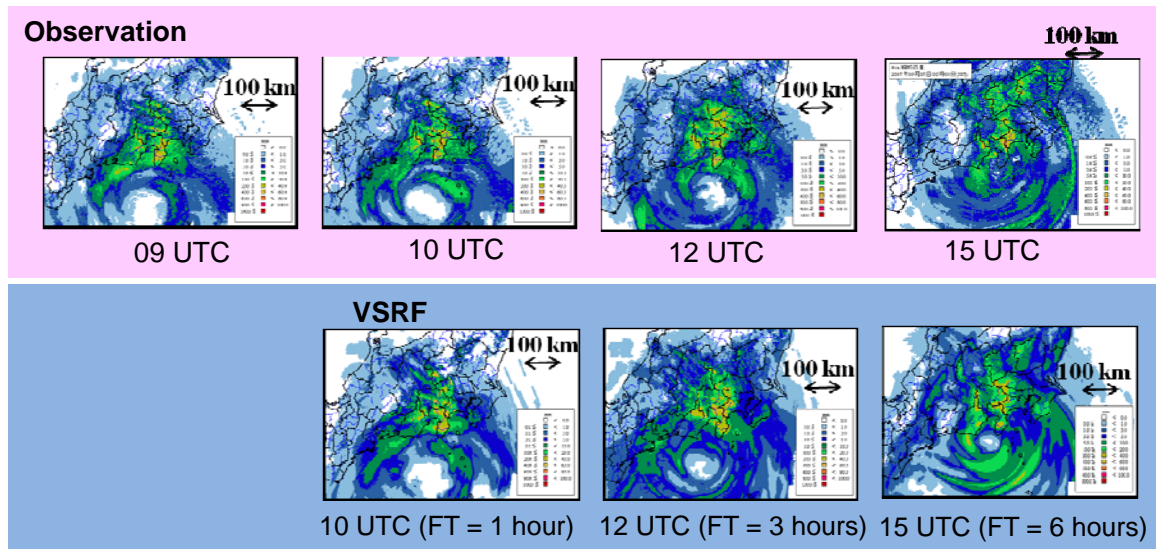


Fig. 8 Sample of VSRF (initial time: 09 UTC, 6 Sep. 2007)

3.1 VSRF algorithms

Generally, extrapolation is the best method of precipitation forecasting for a time frame within a few hours from the present. However, a numerical model gives better performance gradually over time. JMA therefore conducts VSRF by both using extrapolation and merging model output. The procedure for producing VSRF consists of two parts:

1. The extrapolation method
2. The merging method

3.1.1 Extrapolation method

3.1.1.1 Movement vectors

First, the area over Japan is divided into 50-km grid squares. Then, the movement vectors of precipitation systems are estimated for every 50-km grid using a pattern matching method, which indicates the systems' direction and speed of movement. In order to avoid any adverse influence from orographic effects on this estimation¹, time subtractions of R/A are used. Thirty candidates for movement vectors in the grid with the highest matching scores are obtained accordingly using the differences among R/A ($t = 0$ h), R/A ($t = -1$ h), R/A ($t = -2$) and R/A ($t = -3$ h). Then, the most suitable candidate vector is selected in consideration of time-space smoothness. Movement vectors gradually approach the speed of 700-hPa winds of the MSM as the forecast time increases. Figure 9 shows a sample of a movement vector (left) and the one-hour accumulated precipitation forecast with this movement vector (right).

¹ Orographic effects in a grid cause precipitation systems to look static or appear to move more slowly than they actually do.

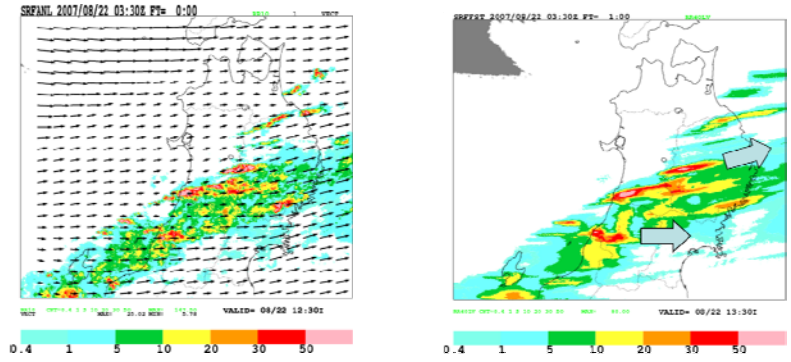


Fig. 9 Sample of movement vectors and forecast one-hour accumulated precipitation
 Left: initial echo intensity (shading) and movement vectors (arrows); right: forecast one-hour accumulated precipitation. The block arrows show precipitation system direction of movement.

3.1.1.2 Orographic effects

Precipitation caused by orographic enhancement is sometimes seen to be stationary over the windward side of mountains. The algorithm follows the concept of the seeder-feeder model (Browning & Hill, 1981). Rainfall passing through a feeder cloud generated by orographic effects becomes enhanced due to water droplets in the feeder cloud.

Precipitable water, which is estimated using data for temperature, relative humidity and wind from the surface to 850 hPa in the MSM, is used to judge whether feeder clouds are generated. If so, precipitation is enhanced depending on the amount of rainfall from the seeder cloud. Figure 10 shows orographic enhancement of precipitation.

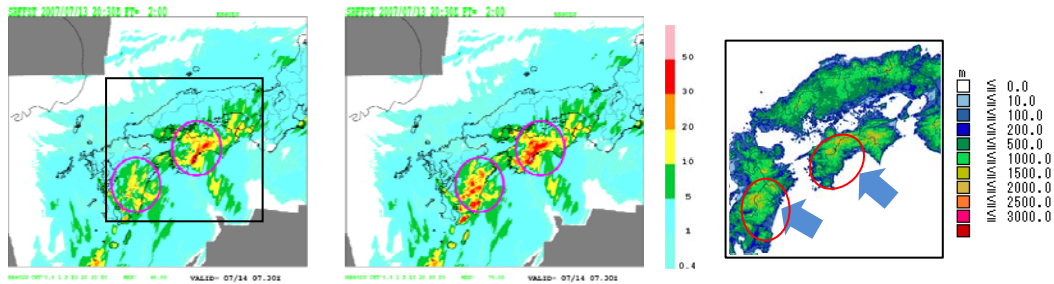


Fig. 10 Orographic enhancement (inside the circles of the figures to the left and center)
 Left: forecast one-hour accumulated precipitation without orographic effects; center: as per the image on the left, but with orographic effects; right: altitude map showing the square area from the figure on the left. The block arrows show precipitation system direction of movement.

The dissipation of echo on the lee side of mountains is also considered. This occurs when the echo top is low, the angle between the directions of mid- and low-level winds is small, and no echoes are present in the dissipation area. Echo dissipation is clearer when echo intensity is stronger and the travel time from the mountaintop to the dissipation area is longer. Echo dissipation is estimated statistically from 700-hPa winds, 900-hPa winds and the relative humidity of the MSM. Figure 11 shows a case of echo dissipation.

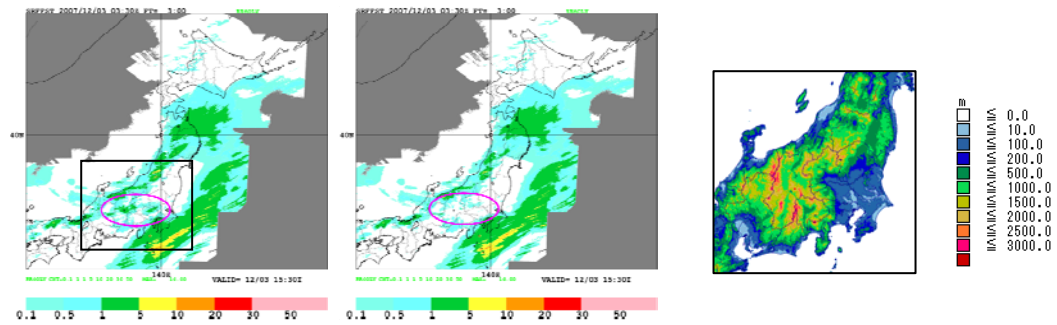


Fig. 11 Echo dissipation (inside the circles of the figures to the left and center)

Left: forecast one-hour accumulated precipitation without orographic effects; center: with orographic effects; right: topographic map with altitude showing the square areas from the figures to the left and center.

3.1.1.3 Accumulation of forecast intensity

The initial field used for VSRF is a composite echo intensity field obtained in the process of making R/A. The echo intensity field is shifted along the movement vector with a time step of two or five minutes. One-hour precipitation at a particular point is calculated as the sum of the echo intensities passing that point. In the process, enhancement and dissipation of precipitation due to orographic effects are considered.

3.1.2 Merging of extrapolation method and MSM

The performance of the conventional extrapolation method is satisfactory up to three to four hours from the initial time. For forecast times of more than six hours, the results of the MSM are considered superior to those of the extrapolation method. It is expected that four- to six-hour forecasts can be improved by merging the results of the extrapolation method and those of the MSM with a different blending ratio over time. The blending ratio is estimated from the accuracy levels of the extrapolation method and the MSM over the past few hours (Araki, 2000). VSRF is the output of this merging process, for which a sample is shown in Figure 12. The precipitation in the red circle for VSRF is from an extrapolation method forecast, and that in the blue circle is from the MSM. R/A more closely corresponds to VSRF than to extrapolation method forecasting and the MSM due to the merging of the extrapolation method forecast and the MSM.

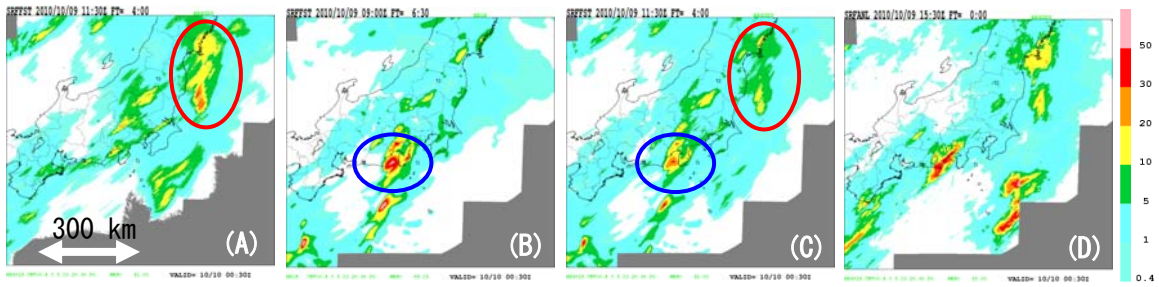
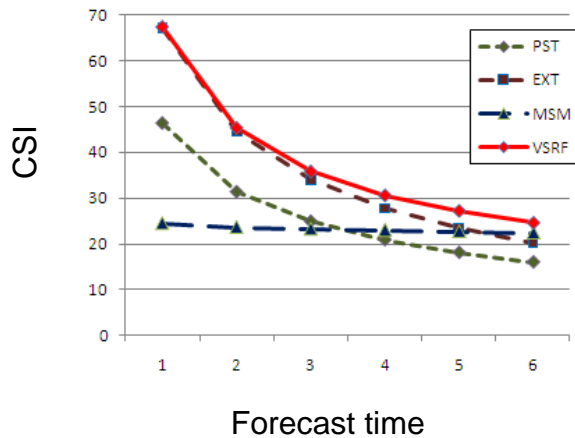


Fig. 12 Merging process

Forecasting with (A) the extrapolation method, (B) the MSM and (C) VSRF for 1530 UTC on 9 Oct., 2010, and (D) R/A for the same time. The initial time of (A) and (C) is 1130 UTC (FT = 4), and that of (B) is 0900 UTC (FT = 6.5). Precipitation in the red circle for VSRF originates from the extrapolation method, and that in the blue circle originates from the MSM. The amount of precipitation depends on the blending ratio.

3.2 Accuracy of VSRF

Critical Success Index (CSI) values for VSRF, the extrapolation method (EXT), the MSM and the persistent forecast (PST) for averaged hourly precipitation from June to August 2010 are shown in Fig. 13. Here, the region over Japan was divided into 20-km grid squares. The threshold of rainfall is 1 mm/hour. The figure shows that VSRF exhibits superior performance over the whole forecast time.



		Event observed	
		Yes	No
Event forecast	Yes	A	B
	No	C	D

$$CSI = A / (A + B + C) \times 100$$

Fig. 13 CSI of VSRF, the extrapolation method (EXT), the MSM and the persistent forecast (PST) verified from June to August 2010

4. Applications of QPE/QPF

Precipitation figures alone do not provide enough information for forecasters to monitor and forecast sediment-related disasters because such events are closely linked to the amount of moisture in the soil. JMA uses the Soil Water Index to monitor and forecast sediment-related disasters.

Precipitation figures alone also provide insufficient information for forecasters to monitor and forecast flood disasters because such events are closely linked to the amount of water outflow to rivers as well as the time lag of water as it moves along river channels. JMA uses the Runoff Index to monitor and forecast flood disasters.

4.1 Soil Water Index

The Soil Water Index (referred to here as the “SWI”) is calculated up to six hours ahead with a spatial resolution of 5 km showing the risk of sediment-related disasters (debris flow, slope failure, etc.) caused by heavy rain. Figure 14 shows a sample of the SWI.

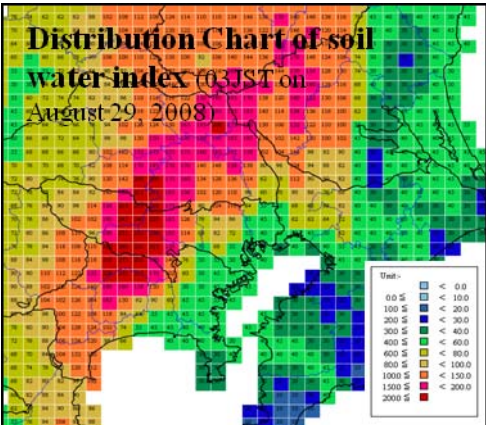


Fig. 14 Soil Water Index distribution chart

The risk of sediment-related disasters caused by heavy rain becomes higher when the amount of moisture in soil increases. Such disasters may sometimes be caused by rainfall from several days before.

The amount of moisture in the soil is indexed using the tank model method to indicate how much rainwater is contained in soil based on rainfall analysis (see Fig. 15). R/A and VSRF are used as input for the tank model.

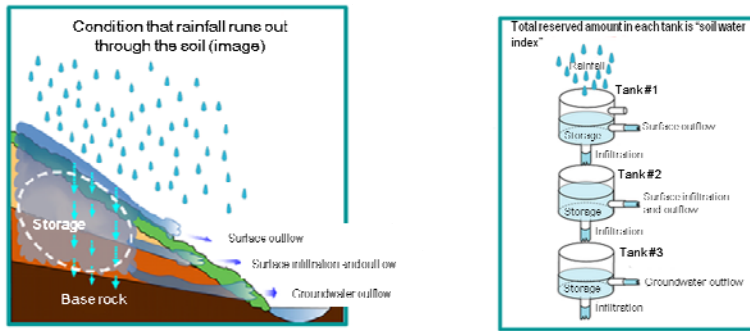


Fig. 15 Outline of tank model

Left: Condition in which rainfall runs out through soil; right: The total reserved amount in each tank is used to form the Soil Water Index.

Sediment-related disasters frequently occur in areas with high SWI values. Figure 16 shows a time-sequence representation of the SWI in a grid where a sediment-related disaster actually occurred. Its timing approximately coincided with the peak SWI value.

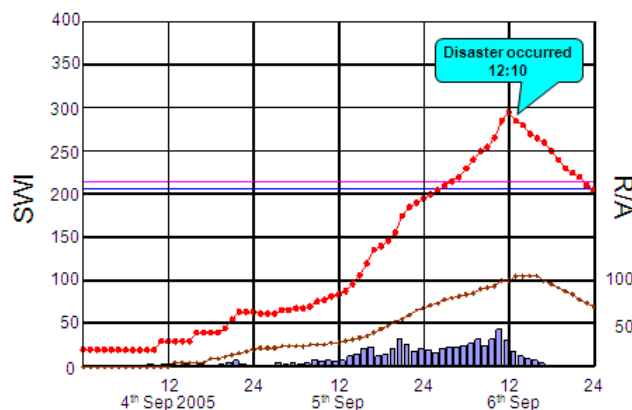


Fig. 16 Time-sequence representation of SWI and rainfall amounts in a grid where a sediment-related disaster occurred. The red line shows the SWI, the brown line shows 24-hour cumulative rainfall, and the bars show 1-hour cumulative rainfall.

Since May 2010, the SWI has been used by forecasters at JMA's meteorological observatories when issuing heavy rain warnings/advisories to call attention to the risk of sediment disasters.

4.2 Runoff Index

The Runoff Index (referred to here as the "RI") is calculated up to six hours ahead with a spatial resolution of 5 km showing the risk of flooding for individual rivers in the country. The amount of rainfall is not directly linked to the risk of flooding for the following two reasons:

1. There is a time difference between the occurrence of rainfall and increased water levels in rivers.
2. It takes time for water to run down river channels.

Accordingly, when monitoring and forecasting flood risk, the above two effects should also be carefully considered in addition to accurate QPE/QPF (see Fig. 17).

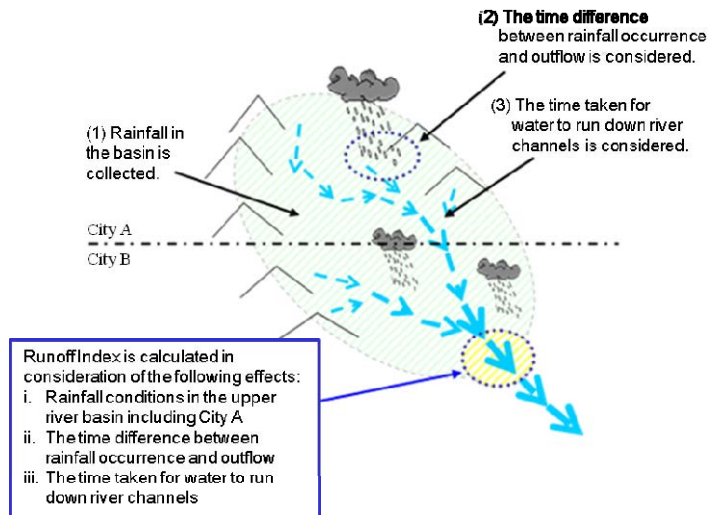


Fig. 17 Three effects to be considered in evaluating flood risk

In the RI, the tank model is used to estimate outflow, and includes the processes of water flowing down the slopes of the basin (covering an area of about 5 km × 5 km) to the river, and then down the river channel. The RI is calculated targeting rivers with a length of 15 km or more. R/A and VSRF are used as inputs for the tank model. Figure 18 shows a sample of the RI.

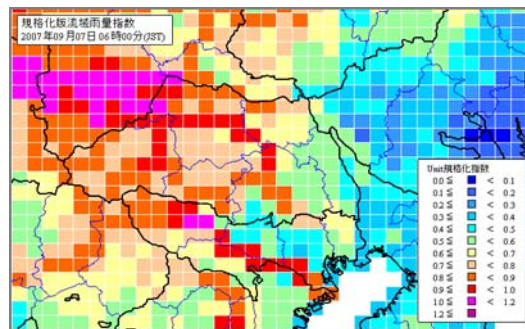


Fig. 18 Sample of the RI shown in 5-km grids

Floods frequently occur in areas with high RI values. Figure 19 shows a time series representation of the RI and water levels in a grid where actual flooding occurred. The time series corresponds closely to the water level of the river.

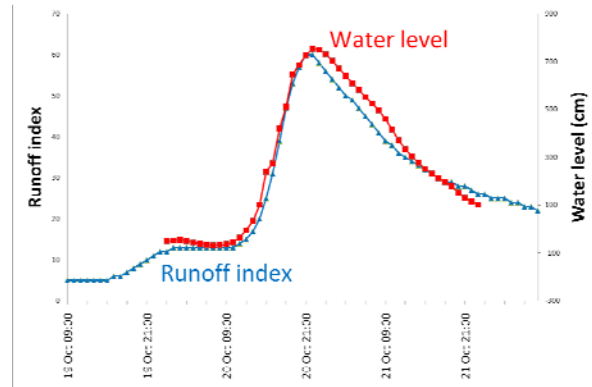


Fig. 19 Time series of the RI and water levels for a grid in which flooding occurred.

The red line shows the water level, and the blue line shows the RI.

Since May 2010, the RI has been used by forecasters at JMA's meteorological observatories when issuing flood warnings/advisories to call attention to the risk of flooding.

References

- Araki, K., 2000: Six-hour forecasts of precipitation. Reports of the Numerical Prediction Division, **47**, 36 – 41 (in Japanese).
- Browning, K. A., F. F. Hill, 1981: Orographic Rain. *Weather*, **35**, 326 – 329.
- Makihara, Y., 2000: Algorithms for precipitation nowcasting focused on detailed analysis using radar and rain gauge data, Study on the Objective Forecasting Techniques, Technical Reports of the Meteorological Research Institute, **39**, 63 – 111.